



ELSEVIER

Contents lists available at ScienceDirect

# Engineering Failure Analysis

journal homepage: [www.elsevier.com/locate/engfailanal](http://www.elsevier.com/locate/engfailanal)

## Thermal fatigue degradation progress in SiMo ductile cast iron under oxidation conditions

M. Terčelj<sup>a</sup>, J. Burja<sup>a,b,\*</sup>, G. Kugler<sup>a,\*</sup>, P. Mrvar<sup>a,\*</sup><sup>a</sup> University of Ljubljana, Faculty of Natural Sciences and Engineering, Askerčeva 12, 1000 Ljubljana, SI, Slovenia<sup>b</sup> Institute of Materials and Technology, Lepi pot 11, 1000 Ljubljana, SI, Slovenia

### ARTICLE INFO

#### Keywords:

Metallurgical engineering  
Exhaust manifolds  
Cast irons  
Casting  
Microscopic characterization and microanalysis  
Thermal fatigue  
Material defect  
Microstructural control

### ABSTRACT

Thermal fatigue tests were conducted on a high Si low Mo ductile cast iron (DCI) under oxidation conditions at 600 °C. The study aimed to understand the evolution of surface degradation, focusing on complex composed graphite nodules, pearlite islets, and their impact on crack initiation and growth in relation to oxidation processes, etc. Degenerated graphite nodules, that include ferrite particles, and areas of increased graphite nodule density, along with pearlite islets, were examined for their oxidation behavior. At lower thermal cycles numbers cracks primarily initiated at the graphite-matrix interface and grew faster in the case of successively arranged graphite nodules and their higher local number density. Graphite degradation involved debonding between graphite and matrix, followed by complex oxidation processes. Degenerated nodules exhibited higher oxidation rates due to the presence of ferrite which acts as oxidation pathways. Areas with increased graphite density and larger sizes facilitated accelerated oxidation via crack formation. Additionally, pearlite degradation started with cracked cementite lamellae, followed by oxidation. Strategies to enhance thermal fatigue resistance included reducing graphite nodule diameter, ensuring their uniform distribution, preventing of formation of degenerated nodules and eliminating porosity. These findings improve understanding of thermal fatigue behavior in DCI that has proven to be even more complex than previously thought. The findings will guide the development of advanced materials for demanding applications.

### 1. Introduction

Due to their acceptable price, excellent castability, good thermal conductivity, and a balanced combination of mechanical properties (strength, ductility, fatigue, and wear resistance), ductile cast irons (DCI) have found widespread application in various industries. These include the automotive industry (for motor blocks, manifolds, exhaust systems, brake drums, crankshafts, and truck axles), wind energy (turbine components), gearboxes, pipeline components (such as valves, fittings, and pipes), and more. The advantages offered by DCI have led to an expectation of further increased applications. However, this necessitates the development of new cast irons with improved properties capable of withstanding higher mechanical, thermal, tribological, and chemical loads over wider temperature ranges. Additionally, there is a need to understand the degradation mechanisms that occur in specific load and environmental conditions [1–8]. Consequently, the application of DCI in harsh oxidation environments subject to thermal fatigue is an area that has received less research and remains poorly understood.

\* Corresponding authors.

E-mail addresses: [jaka.burja@imt.si](mailto:jaka.burja@imt.si) (J. Burja), [goran.kugler@ntf.uni-lj.si](mailto:goran.kugler@ntf.uni-lj.si) (G. Kugler), [primoz.mrvar@ntf.uni-lj.si](mailto:primoz.mrvar@ntf.uni-lj.si) (P. Mrvar).

<https://doi.org/10.1016/j.engfailanal.2023.107823>

Received 27 September 2023; Received in revised form 13 November 2023; Accepted 20 November 2023

Available online 23 November 2023

1350-6307/© 2023 The Authors.

Published by Elsevier Ltd.

This is an open access article under the CC BY license

(<http://creativecommons.org/licenses/by/4.0/>).

Significant progress has been made in the understanding of cast irons in the last two decades, with numerous investigations focused on developing new cast irons with improved properties such as strength, ductility, toughness, hardness, and wear resistance [9–16]. Other areas of research include testing mechanical properties [17–27], thermal–mechanical fatigue resistance [28–39], thermal fatigue resistance [39,42–51], oxidation resistance [8,52–74], and determining the conditions for achieving desirable graphite and matrix microstructures [74–83].

The matrix microstructure in DCI can vary from ferrite to pearlite, as well as from austenite to bainite, and even martensite, in which different graphite morphologies are achieved, such as flake, compacted (vermicular), and spheroidal (nodular) graphite. The matrix microstructure and graphite characteristics decisively influence the relevant properties of cast iron, including static and fatigue strength, thermal conductivity, thermal fatigue resistance, oxidation behavior, and degradation development [3,4,6,9–11,16,27,32,33,39,48–52,56,75–82,83,84].

Studies have focused on the occurrence and growth of microcracks, crack linking, creep, oxidation, and their mutual effects in relation to the aforementioned loads, microstructural characteristics, and graphite characteristics. In the case of mechanical fatigue loads, three different damaging mechanisms related to graphite have been observed: matrix-nodules “pure” debonding, an “onion-like” mechanism, and “disaggregation” [19–21,26–28,38,77]. Nodular graphite is desired for improving mechanical fatigue properties, with their effectiveness depending on chemical composition, inoculation method, graphite nodule size, ferrite content in the matrix, and other factors. Decreased graphite nodularity reduces high-temperature fatigue life and corrosion resistance [39]. On the other hand, compacted and flake graphite are desired for achieving better thermal conductivity and thermal fatigue resistance. Thermal stresses arise from the obstruction of material thermal expansion due to thermal gradients and different thermal expansion coefficients of the individual phases [47]. In recent years, research has focused on high Si and low Mo cast irons designed for high-temperature applications [4,8]. The oxidation resistance of cast iron is vital for high-temperature mechanical and thermal fatigue resistance since oxidation is always involved under such conditions. It has been found that the addition of Cr, Ni, V, Si, Al, Mn, Ce, and La can improve the oxidation resistance of cast iron [4,51,84].

However, the role of oxidation in relation to the characteristics of graphite in thermal fatigue, leading to the deterioration of component surfaces, is an important scientific issue in the industry that has received limited coverage in the literature [44–47,67]. Furthermore, the exact mechanisms of fatigue crack initiation at graphite nodules, especially in new cast iron materials such as Si-DCI, remain largely unknown. Specifically, there is a lack of understanding regarding the mechanical fatigue mechanisms within the graphite itself [78], which also applies to thermal fatigue.

The investigated DCI in this study, is used for exhaust systems. Consequently, thermal fatigue tests were conducted on DCI specimens with an increased Si content (4.34 wt%) under harsh oxidation conditions. The objective was to investigate the degradation mechanism, including the initiation and growth of cracks in relation to debonding and graphite oxidation. The tests were carried out at a maximum temperature of 600 °C, and the testing was interrupted after a selected number of thermal-cooling cycles. This allowed for the observation and explanation of the evolution of degradation in the surface layer of the test specimens, specifically the initiation and growth of cracks in relation to graphite characteristics (density, size, morphology, structure, etc.) and oxidation.

Several references describing the influence of high-temperature working on cast iron have revealed that the most commonly used material is high silicon and molybdenum alloyed cast iron [40,41,68–70]. Depending on the shape of the graphite, it can be used as either spheroidal graphite cast iron or compacted graphite cast iron. The typical silicon content ranges from 4 to 6 wt%, while the molybdenum content ranges from 0.1 to 2 wt%. In some cases, additional alloying elements such as V, Ni, and up to 2 wt% of Cr may be added. One of the most significant influencing elements is silicon, which raises the reference temperature for the solid-state transformation of pearlite into austenite and/or ferrite and graphite into austenite. Molybdenum increases heat resistance through substitutional solid solution and the formation of  $M_{23}C_6$  carbides.

## 2. Experimental

### 2.1. Material

A high silicon and low molybdenum ductile cast iron (DCI) material, belonging to the cast iron family [44–47,67], was used for thermal fatigue testing. The base alloy was produced in a medium-frequency induction furnace with a capacity of 5 tons. The metal charge consisted of recycled cast iron, steel scrap, pig iron, carburizer, ferromolybdenum (FeMo65), and ferrosilicon (FeSi75). Desulfurization was performed by adding calcium carbide ( $CaC_2$ ) in the casting ladle. The magnesium treatment was done by a sandwich process in the casting ladle. The nodulizing agent used was FeSi50Mg15, and the inoculant was FeSi60Ba5. The treated SiMo DCI alloy was cast into standard Y-probes-type II with a thickness of 25 mm at 1330 °C. The composition of our alloy is shown in Table 1.

**Table 1**  
Chemical composition of used cast iron in wt%.

C	Si	Mn	S	Cr	Cu	P	Mg	Ni	Mo	Sn	Al	Fe
3.02	4.34	0.34	0.006	0.034	0.027	0.014	0.046	0.02	0.132	0.012	0.022	rest

## 2.2. Thermal fatigue testing

Thermal fatigue testing was conducted using a Gleeble 1500D thermo-mechanical simulator, specifically within its working cell. Hollow (borehole) specimens were clamped between two copper anvils on both sides (see Fig. 1a). The samples were subjected to conductive heating and internal water cooling, which were controlled by a computer. The temperature of the tested sample was measured using a type K thermocouple that was welded in the middle of the sample's working surface. It took approximately 3 s to heat the samples to the maximum selected test temperature of 600 °C. Subsequently, water cooling and air drying of the samples took approximately 0.6 and 0.5 s, respectively (see Fig. 1b).

Thermal fatigue investigations were carried out on samples after a finite number of cycles, specifically after 200, 500, 1000, 2000, and 4000 heating-cooling cycles. For more detailed information about the testing procedure, please refer to reference [48].

## 2.3. Mechanical and microstructural characterization

Tensile tests were conducted on the DCI samples using an INSTRON 1255 universal tensile test machine with a 500 kN capacity. An extensometer was used to measure the strain during the tests. Microhardness values were determined using a Fischerscope H100 Vickers hardness tester, with a load of HV0.1.

The microstructures were examined using a Carl Zeiss AXIO Imager.A1m light optical microscope. For metallographic image analysis, a NIKON MICROPHOT-FXA optical microscope equipped with a HITACHI HV-C20A video camera and Soft Imaging System analysis software was used. In addition, scanning electron microscopes (SEM) Jeol JSM 6060, Jeol JSM 5610 and FEI Nano SEM from ThermoFisher Scientific were utilized to observe the surface (topology and cracks) and microstructure (oxidation and carbides). Energy-dispersive X-ray spectroscopy (EDS) was employed for elemental analysis of the phases. Furthermore, the microstructures were analyzed with elemental mapping using energy-dispersive X-ray spectroscopy (EDX) in combination with SEM.

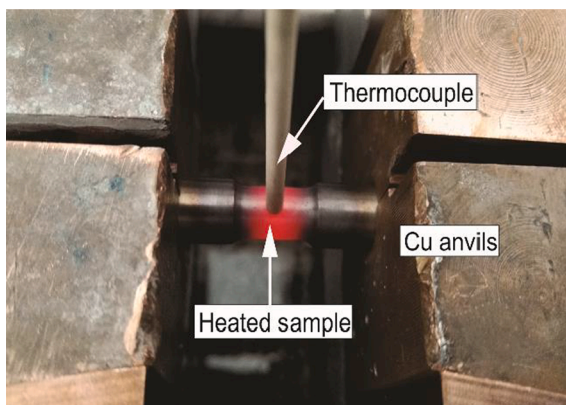
To prepare the surfaces for microstructural evaluation, the samples were ground, polished, and etched with a 3 vol% Nital solution.

## 3. Results and discussion

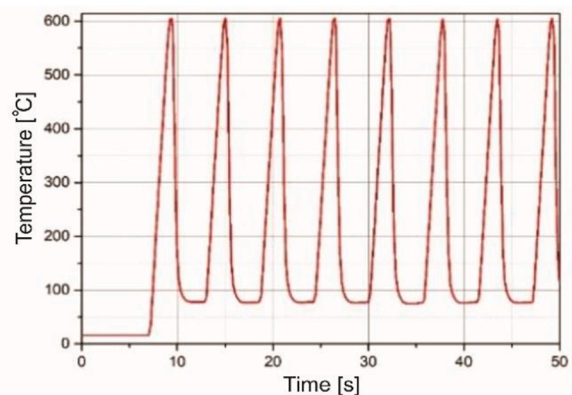
### 3.1. Material description

The microstructure of the DCI material consists of a ferrite matrix, as shown in Fig. 2a (with detail A shown in Fig. 2b), and predominantly nodular graphite, as depicted in Fig. 2b and c. The graphite total area was 11 %, and the metal matrix area was 89 %. Pearlite accounted for 5 % metal matrix area, the carbide network of MxCy 0.2 % of the metal matrix area, and ferrite accounted for 94,8 % of the metal matrix area. (Fig. 2b). Here, MxCy mark alloy carbides with an unknown crystal structure and composition. The graphite/matrix interphase exhibited serrated and hooked features in some cases (Fig. 2b and c). In previous investigations, degenerated graphite was considered as polycrystalline graphite with incomplete spherical shape (less than 100 % nodularity), which was also observed in our study (Fig. 2d). Unexpectedly, a ferritic phase was detected between polycrystalline graphite crystals and within graphite nodules in our case. In fact, the graphite analysis showed that 80 % of the graphite area accounted for fully spherical graphite, 13 % of the graphite area were degenerated (not fully spherical graphite), and 7 % of the graphite area were the degenerated graphite nodules with ferrite particles. Furthermore, the ferrite particles represent around 2–3 % area of the graphite nodules.

Previous studies on thermal fatigue did not specifically focus on this graphite structure. Hence, in our study, the definition of degenerated graphite was expanded to include the mentioned ferrite phenomena, i.e., graphite nodules containing a ferrite phase. Typically, graphite nodules exhibit little to no ferrite or only negligible amounts (Fig. 2c). However, both not fully spherical (Fig. 2d)

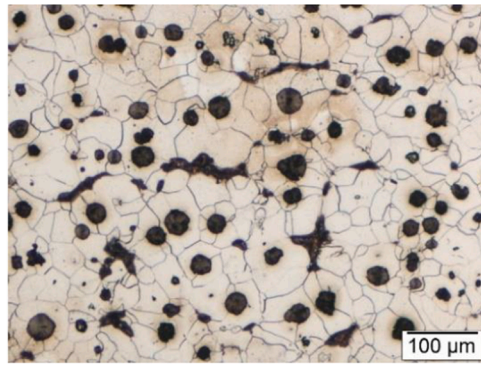


(a)

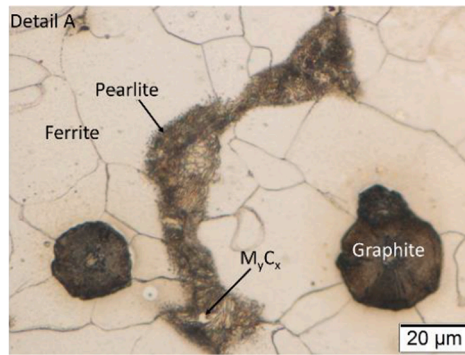


(b)

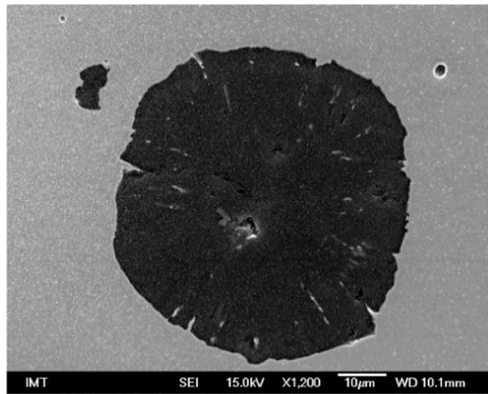
Fig. 1. Test sample and its insertion between copper anvils in Gleeble 1500D working cells (a) and temperature cycles during testing (b).



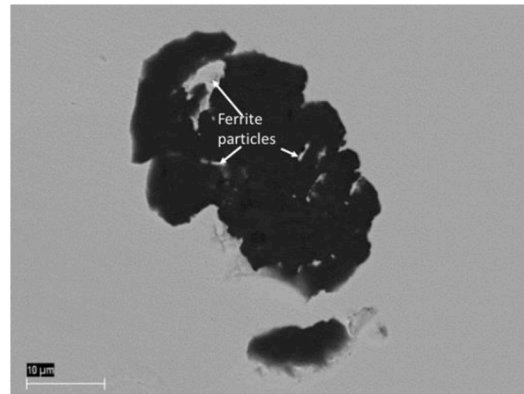
(a)



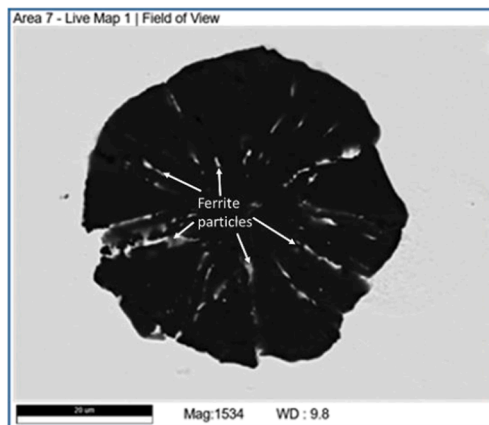
(b)



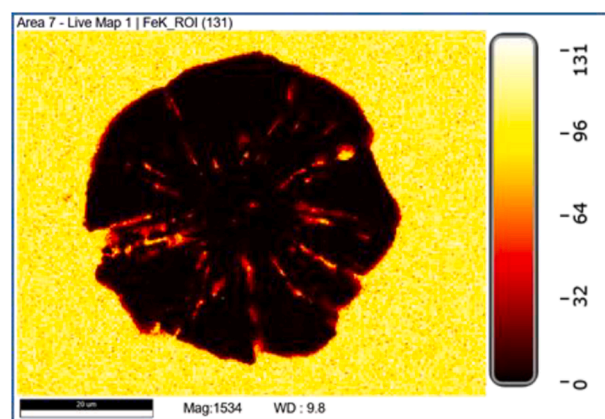
(c)



(d)



(e)



(f)

**Fig. 2.** Microstructure of high Si and low Mo ductile graphite cast iron (a), detail A showing pearlite and  $M_xC_y$  carbides (b) spheroidal graphite containing small amount of ferrite phase (c), not fully spherical graphite (d) and spherical graphite (e) containing increased amount of ferrite phase, EDS mapping for Fe of Fig. 2e (f), images a and b were made with light optical microscope Microphot FXA, Nikon 3CCD, image c was made with Jeol JSM-6500F, image d was made with FEG-SEM ThermoFisher Scientific Quattro S, and images e and f were made with FIB-SEM ZEISS Cross-Beam 550.

and spherical graphite (Fig. 2e) showed also an increased presence of ferrite, as indicated in Fig. 2f, which presents a mapping of Fe within the graphite shown in Fig. 2e.

According to EN ISO 945, the size and distribution of graphite nodules are presented in Fig. 3. The majority of the graphite nodules

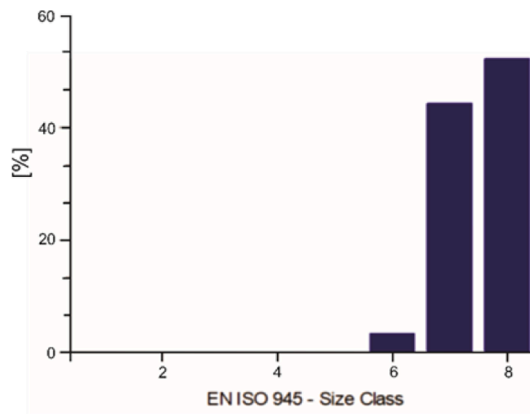


Fig. 3. Size and percentage of graphite nodules estimated according to EN ISO 945.

fall into size classes 7 and 8, while a smaller proportion corresponds to size class 6, with respective area percentages of 45 %, 52 %, and 3 %. The hardness of the prepared DCI material was measured at 255 HB. The average values for tensile strength, yield strength, and elongation were found to be 610.5 MPa, 485 MPa, and 10.5 %, respectively.

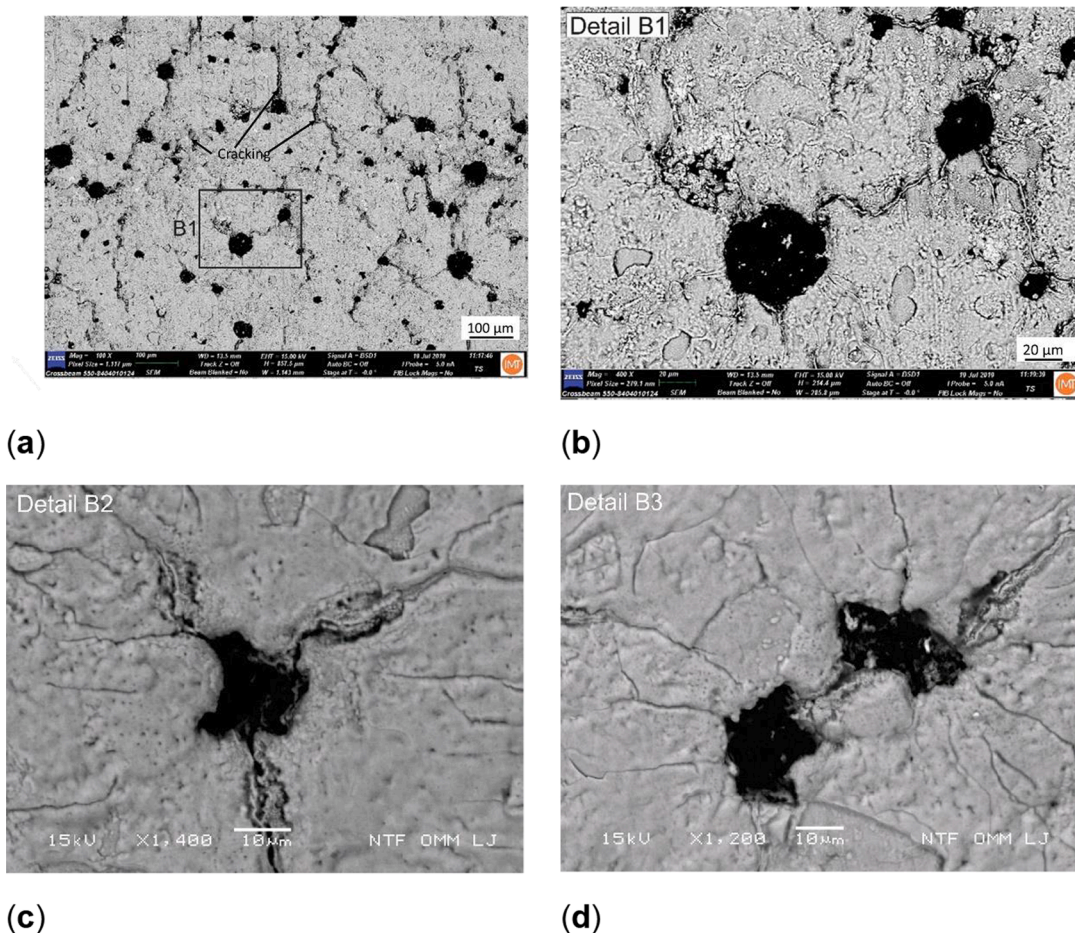


Fig. 4. Appearance of small surface cracks at 200 thermal cycles with denoted **detail B1** (a), **detail B1** (b), **detail B2** of cracks appearance irregular shaped graphite with hooks (c) and **detail B3** of crack between two very close graphite nodules (d), images a and b were made with FIB-SEM ZEISS CrossBeam 550, image c and d were made with Jeol JSM-5610.

### 3.2. Degradation of the surface layer of the test samples

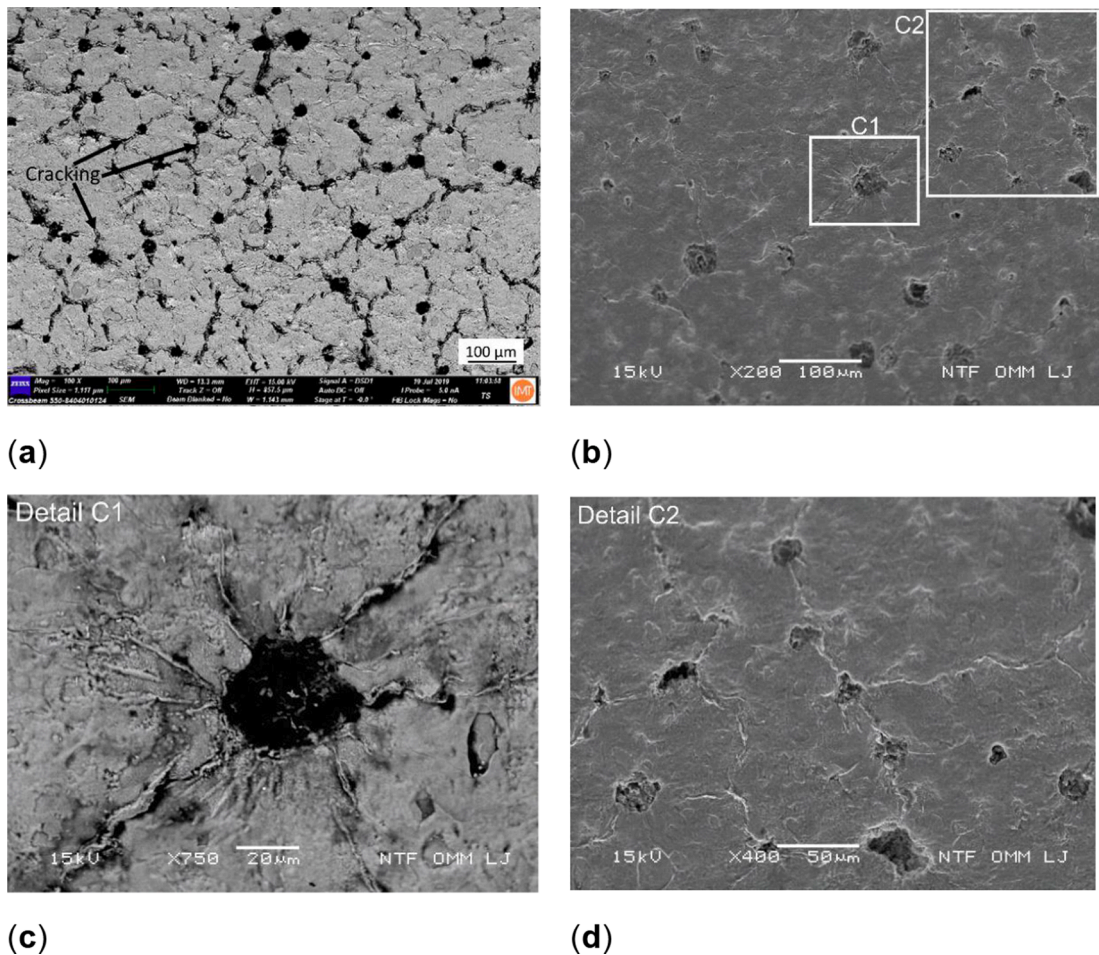
#### 3.2.1. Appearance of cracks on the cooled surface

In thermal fatigue, the characteristic feature is the continuous occurrence of a network of cracks on the surface. This phenomenon is observed in the initial stage, specifically after 200 thermal cycles, as shown in Fig. 4. Fig. 4a highlights the early stage of crack formation at larger graphite nodules, ranging in size from approximately 15 to 60  $\mu\text{m}$  (denoted by the spot, with **detail B1** provided in Fig. 4b). Additionally, microcracks were observed at smaller graphite nodules, particularly at their sharp (hook) shaped areas (see **detail B2** in Fig. 4c). These microcracks are formed due to higher local stress concentrations during thermal cycles. Furthermore, these cracks can link between two graphite nodules that are positioned at a closer distance to each other, as illustrated in **detail B3** of Fig. 4d.

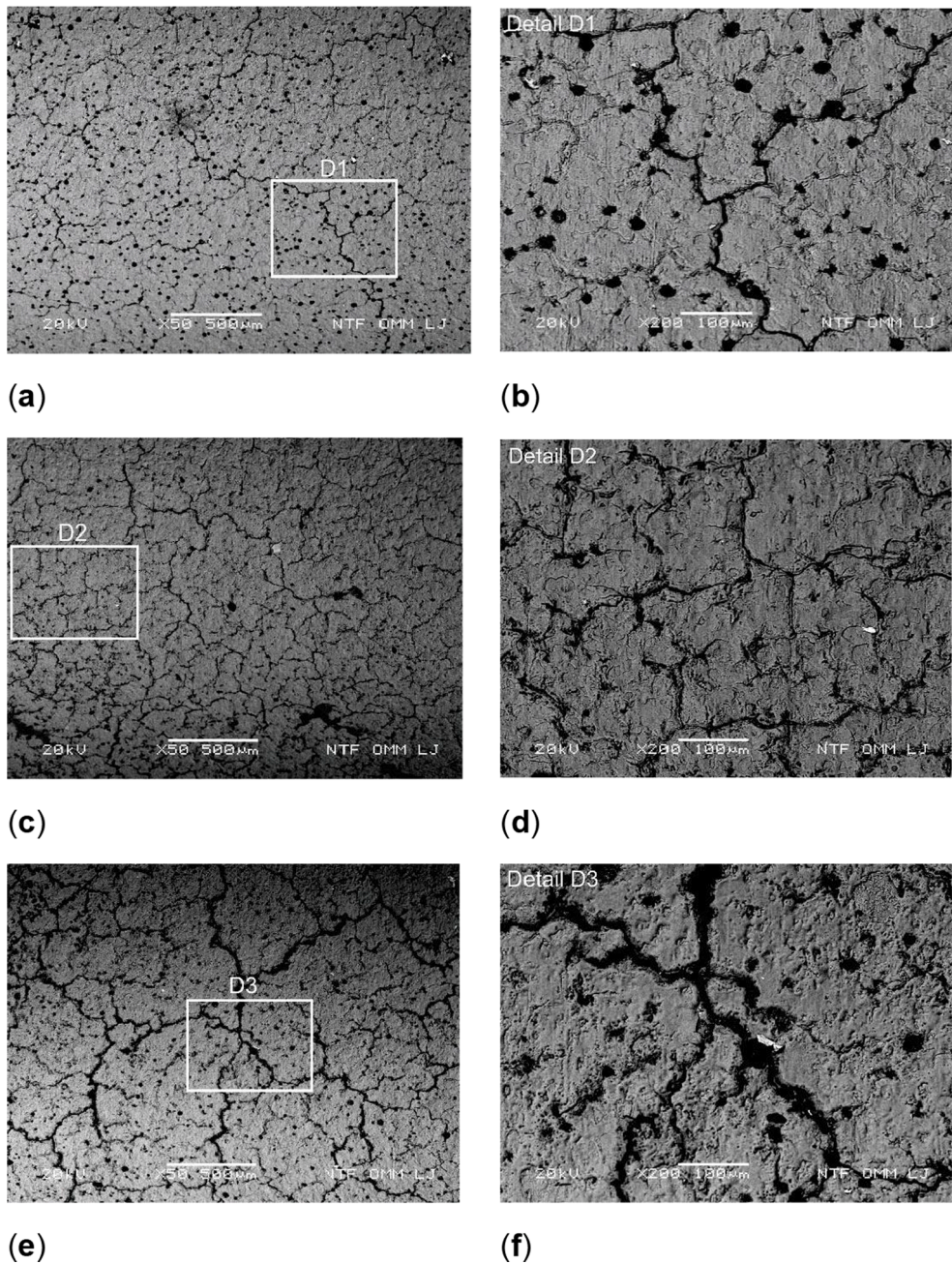
The length and density of cracks increase with the number of cycles, as demonstrated in Fig. 5a for 500 cycles compared to Fig. 4a for 200 cycles. A detailed view of this progression is presented in Fig. 5b. Two specific regions, denoted as C1 and C2, are further examined in Fig. 5c and d, respectively. In Fig. 5c, cracking is observed to intensify around the graphite nodules, indicating a higher susceptibility of these areas to crack formation. Fig. 5d reveals a crack network forming between areas with a higher density of graphite nodules on the surface. In this region, the distance between graphite nodules is smaller, facilitating the linking of cracks into a larger crack. Additionally, cracks originating from the graphite nodules can be seen spreading in other directions. This signifies the initial stage of crack network formation in regions with an increased density of graphite nodules.

Fig. 6a–f illustrates the development of surface cracks at 1000, 2000, and 4000 thermal cycles, along with corresponding **details D1, D2, and D3**, respectively. At 1000 cycles (see Fig. 6a), the initial stage of crack network formation is observed across the entire area, indicating the linking of cracks that originate from clustered or successively arranged graphite nodules. A closer view of this stage is seen in **detail D1** on Fig. 6b.

Moving to 2000 cycles, a denser crack network is evident, and the initiation of secondary cracks can be observed (Fig. 6c). **Detail D2** in Fig. 6d highlights this phenomenon, with secondary cracks appearing at graphite nodules as well as along primary cracks.



**Fig. 5.** Appearance of surface cracks at 500 thermal cycles (a), an increased density and lengths of cracks around graphite (see denoted spots for **detail C1** and **C2**) (b), **detail C1** for cracking around graphite (c) and **detail C2** for linking of cracks between successively arranged graphite nodules that are closer together (d), image a was made with FIB-SEM ZEISS CrossBeam 550, and images b to d were made with s Jeol JSM-5610.



**Fig. 6.** Appearance of surface cracks at different number of thermo-cycles with details; at 1000 cycles (a) with **detail D1** (b), at 2000 cycles (c) with **detail D2** (d) and at 4000 cycles (e) with **detail D3** thermal-cooling cycles (f), all images were made on Jeol JSM-5610.

By 4000 cycles, the linking and continued growth of primary cracks originating from the aforementioned areas are clearly distinguished (Fig. 6e). Additionally, the growth of secondary cracks persists, as depicted in **detail D3** on Fig. 6f.

### 3.2.2. Cross sections of the surface degradation

**3.2.2.1. Degradation process in complex graphite nodules.** As discussed in Chapter 3.1 and illustrated in Fig. 2c–f, it is observed that the graphite nodules can undergo degeneration, characterized by the presence of ferrite islets within the graphite nodules in varying amounts (typically ranging from 0 to 3% in terms of area percentage). The degradation of graphite is influenced by factors such as their depth relative to the cooled surface, composition, size, proximity to cracks, and more.

In the initial stage of degradation, particularly at a low number of cycles (200 thermal cycles), oxidation occurs at the boundary

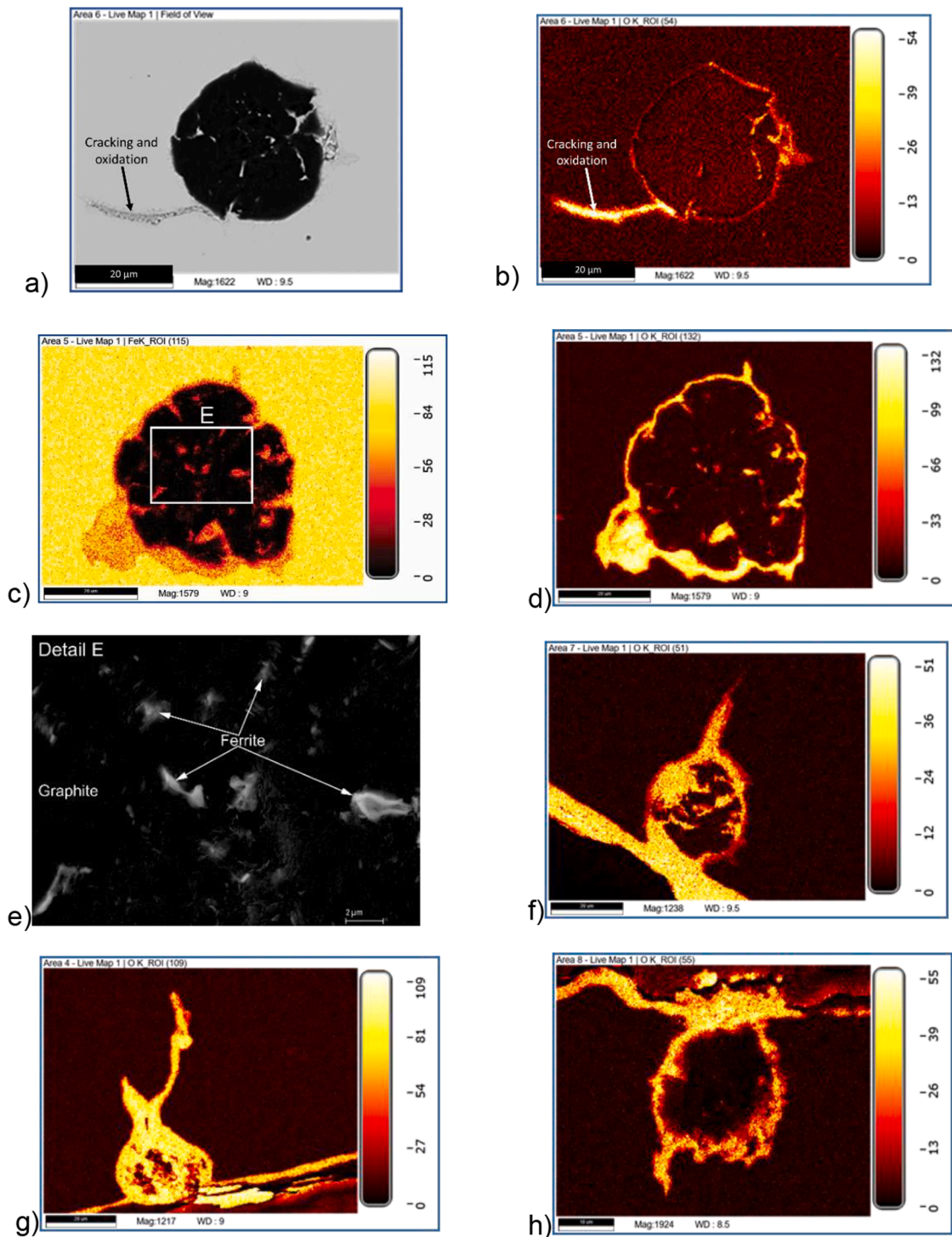


**Fig. 7.** Stages of degradation of degenerated nodular graphite; crack formation and initial oxidation of matrix-graphite boundary around graphite as well as ferrite islets, SEM image (a) and EDS elemental mapping for oxygen at 500 cycles (b), advanced stage of matrix-graphite boundary oxidation around graphite and ferrite islets; EDS elemental mapping for iron (c) and EDS elemental mapping for oxygen with denoted spot for **detail E** at 1000 thermal cycles (d), **detail E** for distribution of ferrite particles in graphite and their initial oxidation of (e) and final stage of complex graphite degradation (oxidation) at 4000 cycles (f-g) and oxidation progress of normal “mono-phased” graphite nodule at 4000 cycles (h) all images were taken of FIB-SEM Zeiss CrossBeam 550.

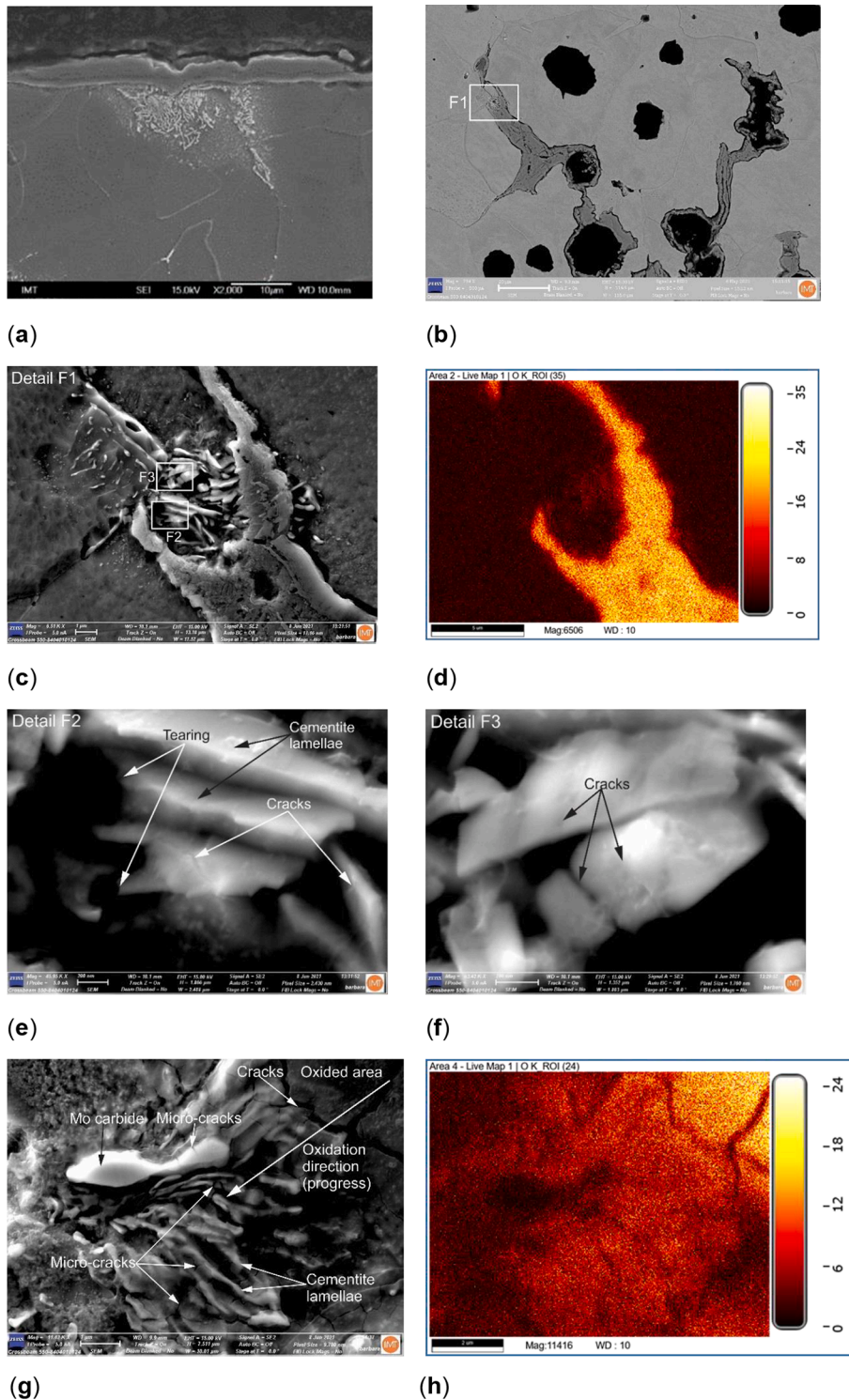


**Fig. 8.** Oxidation behavior of pearlite; slightly increased oxidation rate of some pearlite areas at the cooled surface (a), an increased width of the oxidized crack in the pearlite area (see denoted spot for detail F1)(b), detail F1 with denoted spots for details F2 and F3 (c), EDS elemental mapping for oxygen for detail F1 (d), detail F2 presenting initial cracking (e) and detail F3 presenting advanced cracking of cementite lamellae (f), different stage of oxidized pearlite area (g) and mapping of oxygen for pearlite area given on Fig. 8g (h), image a was made with Jeol JSM 6500F, and images b to h were made with FIB-SEM Zeiss CrossBeam 550.

between the graphite and the matrix, both for normal graphite nodules and degenerated ones. This is followed by the oxidation of ferrite islets within the degenerated graphite, as depicted in Fig. 7a, b. Fig. 7a presents a backscattered electron (BSE) image showing ferrite islets within degenerated graphite nodules, while Fig. 7b shows the elemental energy-dispersive X-ray spectroscopy (EDS) mapping for oxygen. It is worth noting that both oxidation processes (around the graphite and within its internal structure) can occur simultaneously, as evident on the right side of the graphite in Fig. 7b, whereas the ferrite islets, where oxidation has not yet initiated, can be observed on the left side of Fig. 7a.

Subsequent stages of degradation, reflecting the progression of the oxidation process in the afore-mentioned regions, are depicted in Fig. 7c, d. Fig. 7c displays the EDS elemental mapping for iron (Fe), with a denoted spot for **detail E**, and Fig. 7d shows the oxygen mapping. These figures also exhibit crack initiation on the upper side of the graphite (internal side) as a result of increased stresses. **Detail E** in Fig. 7e highlights the complexity of the graphite nodule composition and the initiation of ferrite oxidation. The ferrite particles, with sizes up to 2  $\mu\text{m}$ , are relatively evenly distributed within the graphite. On the other hand, the final stage of nodule oxidation is presented in Fig. 7f–g, focusing on nodules located very close to the cooled surface. It should be noted that the oxidation tongues progress along the pathways provided by the ferrite islets.

The presented figures demonstrate that oxidation initially occurs at the interphase boundaries between graphite nodules and the matrix, followed by simultaneous oxidation of the ferrite areas (islets) within the degenerated graphite nodules. The presence of the ferrite phase within the degenerated nodules serves as pathways that accelerate the internal oxidation of the nodules. The increased volume of oxidized graphite amplifies the stresses around the graphite, thereby further accelerating crack growth, particularly in the radial direction, as evident in Fig. 7c–f. In comparison, for normal graphite nodules (without ferrite islets), oxidation of the interphase boundary area progresses evenly toward the center of the graphite (as shown in Fig. 7h), resulting in increased stresses around the nodules and accelerated crack growth at later stages. This progress of graphite oxidation can be considered as a new finding since this was not described in detail so far. When comparing relevant high temperature oxidation results in literature [4,36,40,45] the slight acceleration of the oxidation front at graphite was noticed, but details of this phenomena were not revealed. In our investigation (i.e. in oxidation environment) the oxidation of graphite nodules is revealed as a more complex behavior, especially in the case of degenerated graphite nodules (presence of ferrite phase), i.e. oxidation begin at boundary between graphite and matrix followed by penetration of oxidation in graphite nodules using ferrite phase particles as pathways that accelerate the oxidation progress.

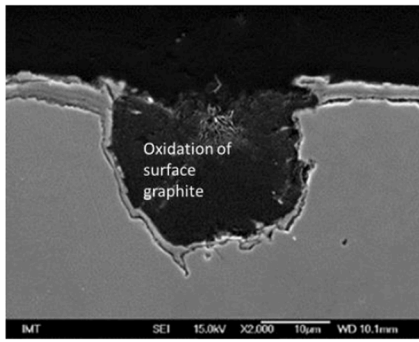
**3.2.2.2. Degradation in pearlite islets.** The degradation processes were less frequently observed in the presence of pearlite due to its lower fraction. However, in some cases, the presence of pearlite on the cooled surface was found to slightly accelerate the oxidation process, as depicted in Fig. 8a. Note that in the interior of the sample when crack growth occurred through a pearlite area we observed the oxidation of the entire pearlite area. This resulted in a significantly increased width of the oxidized crack, as illustrated in both cases in Fig. 8b. **Detail F1** in Fig. 8c highlights the observed phenomenon, and Fig. 8d shows the corresponding elemental mapping for oxygen.

In Fig. 8c, denoted spots for **details F2** and **F3** are provided in Fig. 8e and 8f, respectively. Both figures exhibit cementite lamellae within the pearlite, where cracking and tearing of the cementite lamellae can be observed, indicating the initial stage of pearlite degradation. This cracking and tearing can be attributed to the oxidation process in the vicinity (indicated by the oxidation tongues in Fig. 8d) and the increased stresses resulting from the increased volume of oxidized pearlite in the area. Fig. 8e, f highlight the cracking and tearing of cementite lamellae caused by these factors.

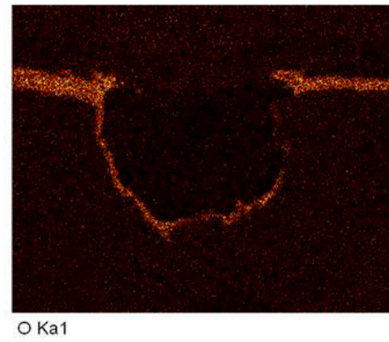
Fig. 8g displays a late-stage oxidized pearlite area, particularly visible in the upper-right area. It is worth noting that the oxidation process of ferrite between cementite lamellae is more pronounced compared to the oxidation of cementite lamellae, while the carbides in the vicinity exhibit less progression of oxidation. Fig. 8h presents the elemental mapping for oxygen in the selected pearlite area shown in Fig. 8g. The increased oxygen content in the upper right region (associated with increased cracking) and the lower values in the lower left region (associated with decreased cracking) clearly indicate the direction of oxidation progression, from the upper right to the lower left, as indicated by the arrow in Fig. 8g. Thus, in fully oxidized areas, cracks are observed with increasing length, while in partially oxidized areas, partially oxidized cementite lamellae and small cracks can be seen in the cementite lamellae as well as in the material between the lamellae. The presence of small cracks in pearlite areas also accelerates their oxidation progress, while the oxidation rate of the material between the cementite lamellae appears to be slightly higher compared to the cementite lamellae themselves.

It is important to note that the oxidation of pearlite at 600 °C does not lead to decarburization, since the oxidation of carbon is not preferred over iron. Furthermore, ferrite is more susceptible to oxidation than cementite. The oxidation of cementite is also discussed later on in “3.3.2. Role of pearlite in crack growth”.

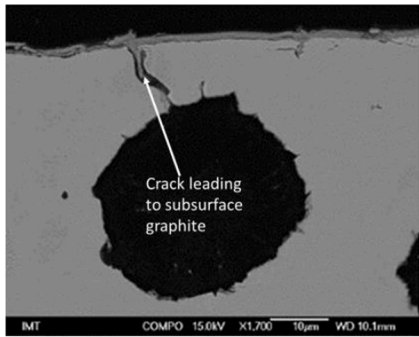
Oxidation of pearlite starts at the grain boundaries, when the oxidation times are long enough both ferrite and cementite lamellae are oxidized. As the oxidation continues ferrite is preferentially oxidized. This creates a rough surface that creates mechanical stresses due to the iron oxide formation, further promoting the oxidation of ferrite and cracking of cementite [85]. Furthermore, the coarser the pearlite the higher the stresses in the oxide layer [86]. Pearlite areas are higher in carbon and alloying elements, that is why carbides more frequently precipitate here. The alloying element carbides, like Cr and Mo carbides, are even more oxidation resistant than cementite. But while the pearlite lamella structure induces stress and cracking during oxidation, the role of alloying element carbides differs. They are precipitated along the grain boundaries, and do not induce stress, but instead they deplete the surrounding area of oxidation resistance enhancing elements like Cr and Mo. Thus they increase the vulnerability to oxidation, especially along the grain boundaries [49]. On other hand Ghodrati et al. [66] reported on the decomposition of pearlite matrix (at elevated temperature oxidation) accompanied by the formation of graphite and oxides, which lead to an increase of material volume.



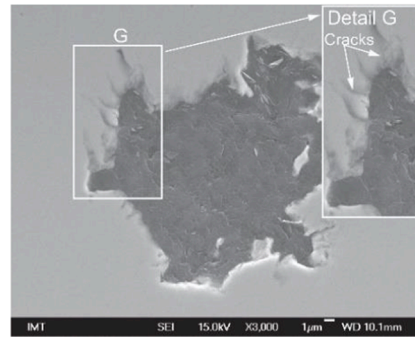
(a)



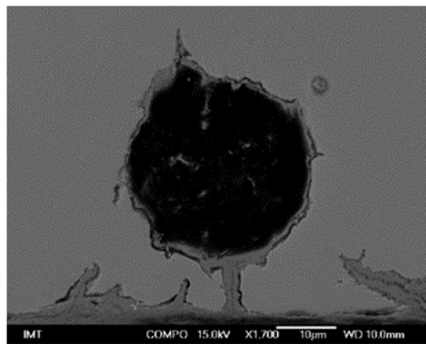
(b)



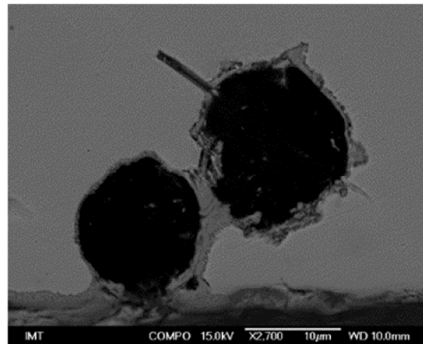
(c)



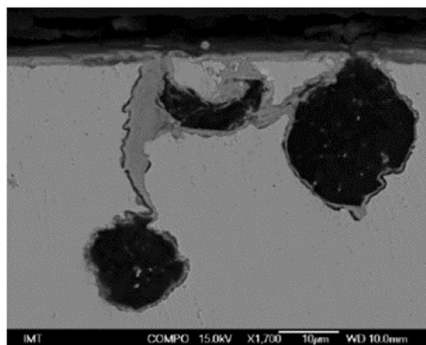
(d)



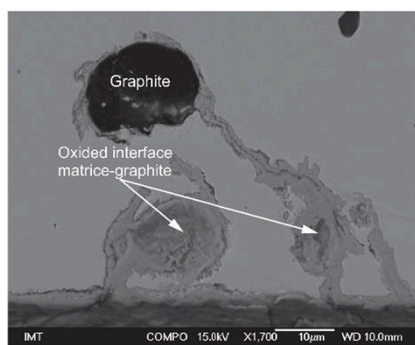
(e)



(f)



(g)



(h)

(caption on next page)

**Fig. 9.** Degradation at 200 thermal cycles: Oxidation of interphase graphite-matrix around graphite (a) with EDS elemental mapping for oxygen (b), the initial stage of crack formation from surface to the graphite hook (c), emphasized cracking of the matrix at hooks (see **detail G**) on the graphite (d), crack formation interconnecting the graphite nodules below surface (e), cracking and oxidation of area between two closer nodules (f), formation of cracks and oxidation between nearby graphite nodules on area with their increased number density (g-h), 200 thermal cycles, all images were made with Jeol JSM 6500F.

**3.2.2.3. Degradation of the surface layer at 200 thermal cycles.** At 200 thermal cycles, the graphite located at or very close to the surface undergoes three typical oxidation stages. Firstly, there is the initial oxidation of the graphite-ferrite boundary areas, primarily on graphite nodules located on the cooled surface. In some cases, small oxidation hooks are also formed, as illustrated in Fig. 9a, b. Secondly, cracks form from the cooled surface to the tops of serrated graphite nodules located very close to the surface, as shown in Fig. 9c. These cracks are a result of higher local stresses generated at each individual top of the serrated spot of the graphite. Fig. 9d provides an additional explanation of increased local matrix cracking (see **detail G** in Fig. 9d) by showcasing spots with hooks of noncircular graphite. Microcracking decreases on the smooth parts of the surface areas of the graphite nodules. A similar situation can be observed on the lower side of the graphite nodule in Fig. 9c, where cracking occurs on serrated spots. However, no oxidation is yet observed around the graphite-matrix boundary.

The next stage of the degradation process is depicted in Fig. 9e, showcasing the formation of cracks leading to graphite nodules that allow the entrance of oxygen. Oxidation occurs at the graphite-matrix boundary as well as within the ferrite islets within the graphite. Cracks (oxidation hooks) also form on the graphite. Furthermore, the formation of oxidation tongues from the surface oriented towards the graphite can be observed, as the graphite nodules represent stress concentrations.

Fig. 9f demonstrates increased oxidation of the area between two nearby graphite nodules. This increased oxidation is also evident in Fig. 9g, where three nearby graphite nodules are oxidized, with one of the nodules being a sharp-edged vermicular graphite type and oriented towards the cooled surface. The sharp spots generate stress concentration, enabling the formation of cracks towards the cooled surface. Cracks also occur between two nodules due to their short distance (approximately 6–7  $\mu\text{m}$ ). As a result, oxidation connects between the graphite nodules, leading to an increased oxidation area on the surface layer and the formation of cracks in the radial direction along the graphite pathways (Fig. 9h). Therefore, the cracking and oxidation are closely related to the density of graphite nodules in a small area, their mutual distance, and shape.

**3.2.2.4. Degradation of the surface layer at 500 thermal cycles.** During testing in the range of 200–500 thermal cycles, further oxidation of graphite nodules near the cooled surface occurs, along with oxidation of the graphite-ferrite boundary (interface) and the formation of oxidation hooks, primarily on the upper side of the graphite (in the radial growth direction). Fig. 10a, with detail H showing oxygen EDS elemental mapping, demonstrates this phenomenon. It is important to note that the nodule in **detail H** is not degenerated (i.e., it is mono-phased), as no internal oxidation of graphite is visible. Consequently, the oxidation rate of the graphite decreases, resulting in reduced stresses in the vicinity that do not contribute to the acceleration of crack growth.

Fig. 10b presents the oxygen EDS elemental mapping of a nodule near the cooled surface, where the formation of oxidation hooks on the upper side of the graphite is visible. These hooks enable further crack growth. Oxidation is visible on the right side of the oxidized graphite grain boundaries, leading to their de-cohesion. Thus, oxidation can progress through the matrix as well as using grain boundary pathways. This is also evident in the case of the large graphite nodule shown in Fig. 10c, where oxidation hooks follow both the grain boundary and matrix pathways. Additionally, signs of debonding can be observed on the upper left side of the figure. Fig. 10d provides an oxygen mapping showing the second stage of oxidation of degenerated graphite, with an increased width of the oxidation band around the graphite (in comparison to Fig. 9b and 9e) and the formation of cracks on the top of the graphite (in the radial direction). These cracks can grow radially to the adjacent graphite nodules in the vicinity. This is further illustrated in Fig. 10e, f, showcasing the formation of cracks in the radial direction for successively arranged graphite nodules. Both figures demonstrate that longer cracks are formed when cracks are initiated early on spots with denser precipitated graphite and their successive arrangement.

In graphite nodules below the surface, no significant changes were observed at the graphite-matrix interfaces. However, in the case of rarely occurring graphite nodules with hooks, increased cracking was observed in the matrix around or at the graphite hooks (see Fig. 10g). Moreover, in graphite nodules with accentuated hooks oriented toward the cooled surface, cracks formed from the surface, leading to an oxidation process in the graphite-matrix interface (Fig. 10h).

The main difference in the degradation process, shown in Fig. 9 for 200 cycles, is the increased number of oxidized graphite at the surface and in close proximity to the surface, along with their oxidation progress through grain boundary pathways.

**3.2.2.5. Degradation of the surface layer at 1000 thermal cycles.** During testing in the range of 500–1000 thermal cycles, further degradation progress was observed. This includes the oxidation of graphite nodules at the cooled surface (Fig. 11a), the connection of oxidation crack networks with graphite nodules (Fig. 11b), the connection of surface cracks to subsurface graphite nodules (Fig. 11c), debonding of graphite nodules in the interior (Fig. 11d, this phenomena was also observed at mechanical fatigue [19,21,22,40]), the oxidation of debonded graphite nodule surfaces, and cracking around them (Fig. 11e). Additionally, the propagation of internal cracks through grain boundary oxidation and their linking with debonded graphite nodules in the vicinity was observed (Fig. 11f). Graphite nodules and their specific arrangement serve as possible initiation sites for further crack growth, both on the surface and subsurface.

However, there are many individual debonding slits that form around the nodules, which can even cause internal cracking, especially in areas with a higher density of graphite nodules. The internal cracks tend to be more intergranular, while the surface cracks do not always follow the grain boundaries and can also be transgranular.



**Fig. 10.** Degradation at 500 thermal cycles; oxidation of interphase boundary graphite-ferrite around graphite and additional formation of oxidation hooks predominately oriented in radial direction with **detail H** for EDS elemental mapping of oxygen (a), EDS elemental mapping for oxygen; oxidation of a surface graphite nodule with visible oxidation along the grain boundaries (b), debonding of graphite nodules in the matrix (c), EDS elemental mapping for oxygen shows increasing oxidation around graphite nodules (d), formation of radial cracks through successively arranged graphite nodules (e f), cracking of matrix at hooked nodule edges (g) and EDS elemental mapping of crack formation at serrated and hooked graphite surface (h), 500 thermal cycles, images a, b, d and h were made with FIB-SEM Zeiss CrossBeam 550, images c, e and g were made with Jeol JSM 6500F, and image f was made with FEG-SEM ThermoFisher Scientific Quattro S.

The occurrence of debonding is influenced by the depth of the graphite nodules and the number of thermal cycles. Initially, debonding was observed after 1000 thermal cycles at a depth of approximately 350  $\mu\text{m}$ . This can be attributed to higher thermal stresses in this depth area, as well as the number of thermal cycles. Specifically, at higher numbers of cycles, the phenomenon of debonding was observed in deeper areas where lower thermal stresses are generated.

**3.2.2.6. Degradation of the surface layer at 2000–4000 thermal cycles.** During the test period exceeding 1000 thermal cycles, the process of further oxidation of both degenerated and normal graphite nodules near the cooled surface continues (Fig. 12a for 2000 cycles and Fig. 12b for 4000 cycles). The oxidation rate of degenerated graphite nodules located at the cooled surface is higher compared to normal graphite (compare oxidation progress in Fig. 12a, b).

Moreover, oxidation around graphite nodules located below the cooled surface was also observed (Fig. 12b, c). This occurs due to the debonding of the graphite-matrix boundary, which accelerates the oxidation of the graphite surface layer in these areas. When external cracks propagate through the debonding area and are close to the cooled surface, the oxidation process is further intensified (Fig. 12b). This effect is particularly pronounced when the graphite nodules are arranged successively, leading to the formation of internal cracks and accelerated crack growth in that direction (Fig. 12b).

Additionally, the formation of secondary cracks leading to graphite nodules in deeper areas was observed (Fig. 12d). In areas with a higher density of graphite nodules, further local crack growth and oxidation occur (Fig. 12e, f for 2000 and 4000 cycles, respectively).

### 3.3. Specifics at growth of cracks and conditions for the formation of longer cracks

#### 3.3.1. Specifics of growth at successively arranged graphite nodules

The degradation process during 1000 thermal cycles is presented in Fig. 13a, where external cracks propagate radially from subsurface graphite nodules that are arranged successively (**details I1** and **I2** in Fig. 13a). Furthermore, **details I3–I5** on the same figure show the occurrence of internal cracks along grain boundaries.

Crack initiation from areas with a higher density of graphite nodules is also frequently observed, as shown in Fig. 13b–d. Tensile stresses and volume expansion due to oxidation around the area lead to crack growth, particularly in the radial direction, especially when graphite nodules are arranged successively. This results in accelerated growth of longer cracks in the radial direction (Fig. 13c, d for 2000 and 4000 cycles, respectively). The initial growth of cracks is characterized by crack propagation from one graphite nodule to the next, predominantly through transgranular cracking. In the interior, at depths of 300–400  $\mu\text{m}$  and deeper, intergranular cracking is visible (**detail I3** in Fig. 13a), which can be attributed to lower thermal stresses. In fact, a combination of both intergranular and transgranular cracking modes can be observed. When a grain boundary is in close proximity to the crack tip, the crack growth can take an intergranular pathway. Therefore, crack propagation can be versatile and dependent on the density of nodules and the proximity of grain boundaries to the crack tip. The crack growth process is a combination of intergranular and transgranular growth (Fig. 13a, **details I3–I5**).

Moreover, **detail I6** in Fig. 13d shows rapid crack growth due to the presence of closely arranged and debonded graphite nodules, where oxidation also occurs. The debonding of the entire area with a high density of nodules leads to internal crack formation, and the sudden entrance of oxygen results in a more uniform oxidation progress of all the included nodules.

Thus, the cracking process depends on the distribution and size of graphite nodules, while the presence of grain boundaries in the vicinity of crack tips determines whether cracking is intergranular or transgranular. Increased crack growth rates can be expected in cases where there are similar orientations of successively arranged grain boundaries (**detail I3**) along the crack growth pathway, as well as in cases of successively arranged graphite nodules (Fig. 13c–d).

In Fig. 14a, crack initiation in an area with an increased density of graphite nodules is shown (**detail J1** in Fig. 14b). Crack growth between two graphite nodules in the radial direction through both intergranular and transgranular cracking is depicted in Fig. 14c (**detail J2**). Fig. 14d (**detail J3**) shows a crack that has propagated between several closely arranged graphite nodules that are almost touching, similar to **detail I6** in Fig. 13d. In Fig. 14d, the initiation of graphite nodule oxidation close to the main crack and the formation of secondary cracks to the graphite are also visible.

**Details J4** and **J5** in Fig. 14e and 14f, respectively, illustrate the growth of cracks from one graphite nodule to another using both grain boundary and transcrystalline pathways. In Fig. 14f, the growth of a crack through an intracrystalline pathway to a graphite nodule before the crack tip is visible, as the presence of graphite creates stress concentrations. Additionally, the initiation of oxidation of graphite nodules in their close proximity before the crack tip can be observed, leading to an accelerated growth rate of the crack as it propagates through this area.

The growth of cracks occurs from one graphite nodule to the next in both radial and oblique directions, influenced by stress concentrations around the graphite nodules. The size of the graphite nodules and their density, as well as their mutual distance, play a

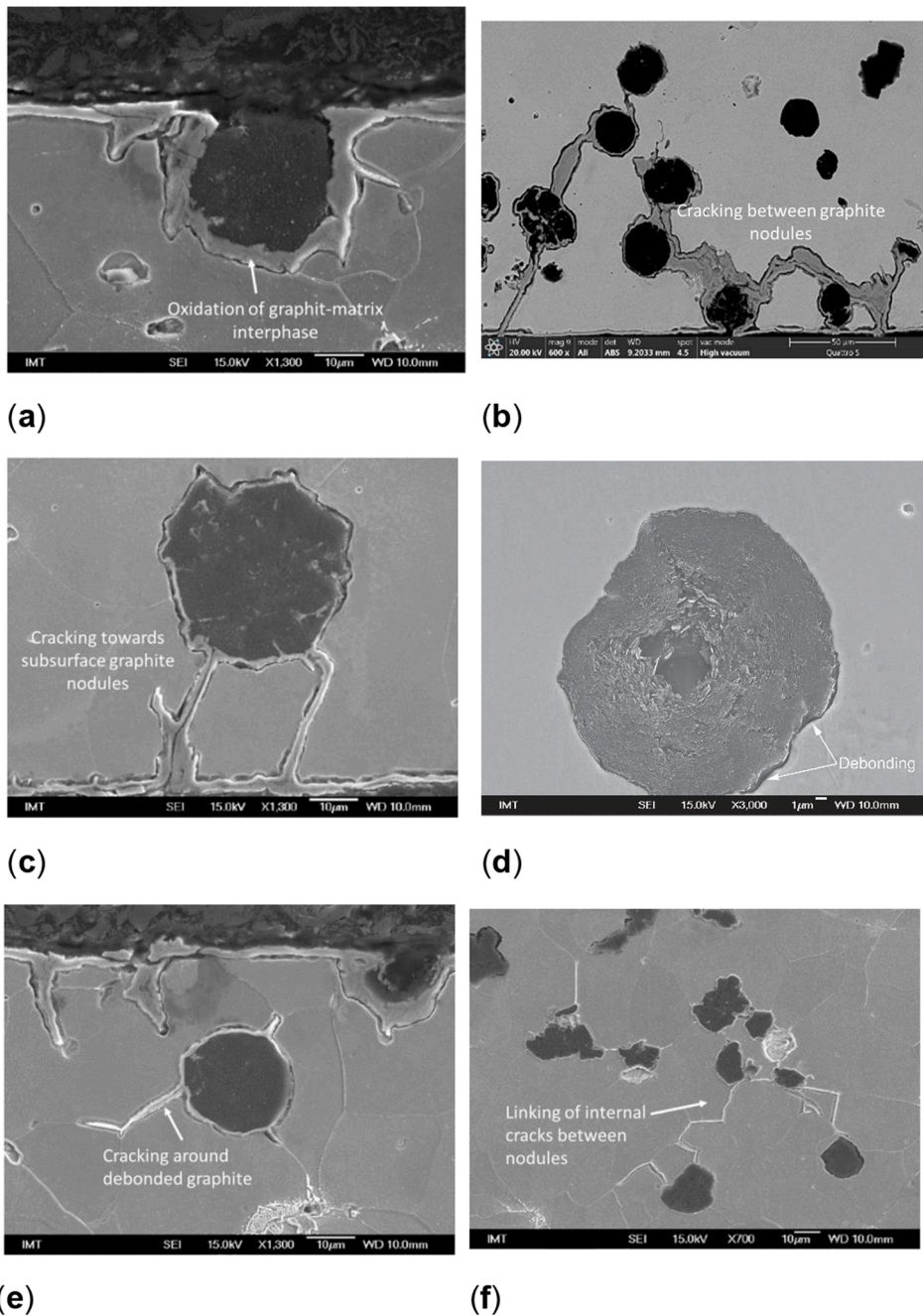


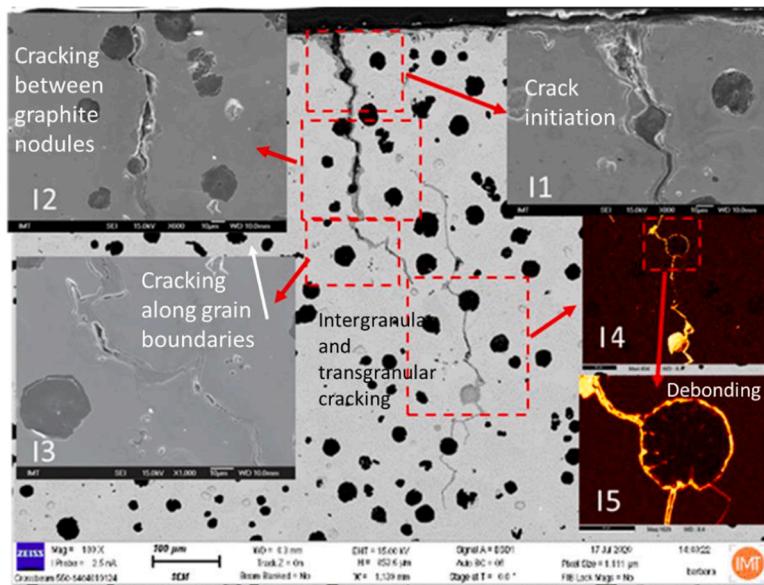
**Fig. 11.** Degradation at surface layer at 1000 thermal cycles; increasing of oxidation band on graphite-matrix interphase (a), formation of cracks between nearby graphite nodules and their oxidation (b), further progress of cracks toward subsurface graphite nodules (c), debonding of graphite nodules (d) and formation of internal cracks around previously debonded graphite nodules initiated at grain boundaries (e), linking of internal cracks between graphite nodules in the vicinity and oxidation of the cracks (f), 1000 cycles, images a, c and d were made by Jeol JSM 6500F, image b was made by FEG-SEM ThermoFisher Scientific Quattro S.

role in crack propagation. The pathway the cracks take, whether grain boundary or transcrystalline, depends on the vicinity and orientation of grain boundaries.

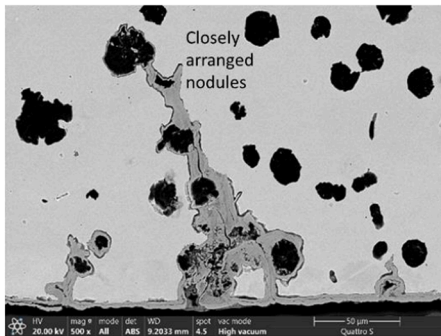
In deeper areas, where thermal stresses are reduced, the role of oxidation in crack growth becomes more significant.

Crack growth and oxidation are accelerated in case of successively arrangement of graphite nodules as well as in case of their local denser distribution in matrix. Furthermore, both mentioned processes are related also with debonding between graphite nodules and matrix that was already observed at lower number of thermal cycles (see Fig. 10d, 11d, 12b). As mentioned above debonding was studied at mechanical fatigue testing [19,21,22,40] while this was not studied in relation to crack growth and oxidation in case of

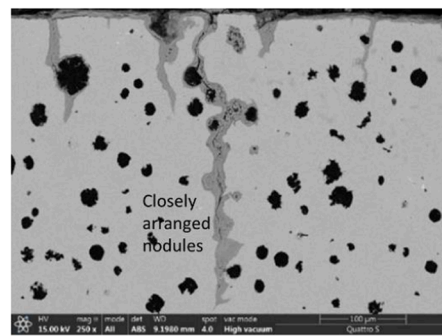




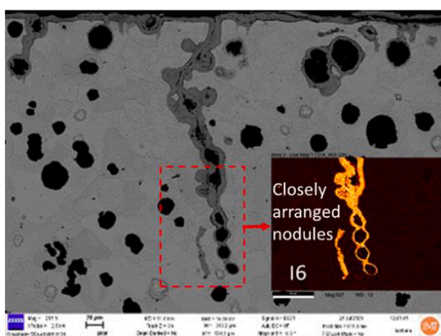
(a)



(b)



(c)



(d)

**Fig. 13.** Growth of cracks; appearance of external and internal cracks with denoted spots for **details I1 – I5** and initiation of crack from area with increased density of graphite nodules (a), initiation of crack on spot with increased density of nodulus (b) and growth of cracks in case of cracks in case of successively arranged graphite nodules, rapid oxidation in closely arranged nodules shown in **detail I6** (c-d), image a was made with FIB-SEM-Zeiss CrossBeam 550 and Jeol JSM 6500F, images b and c with FEG-SEM ThermoFisher Scientific Quattro S, and image d with FIB-SEM Zeiss CrossBeam 550.

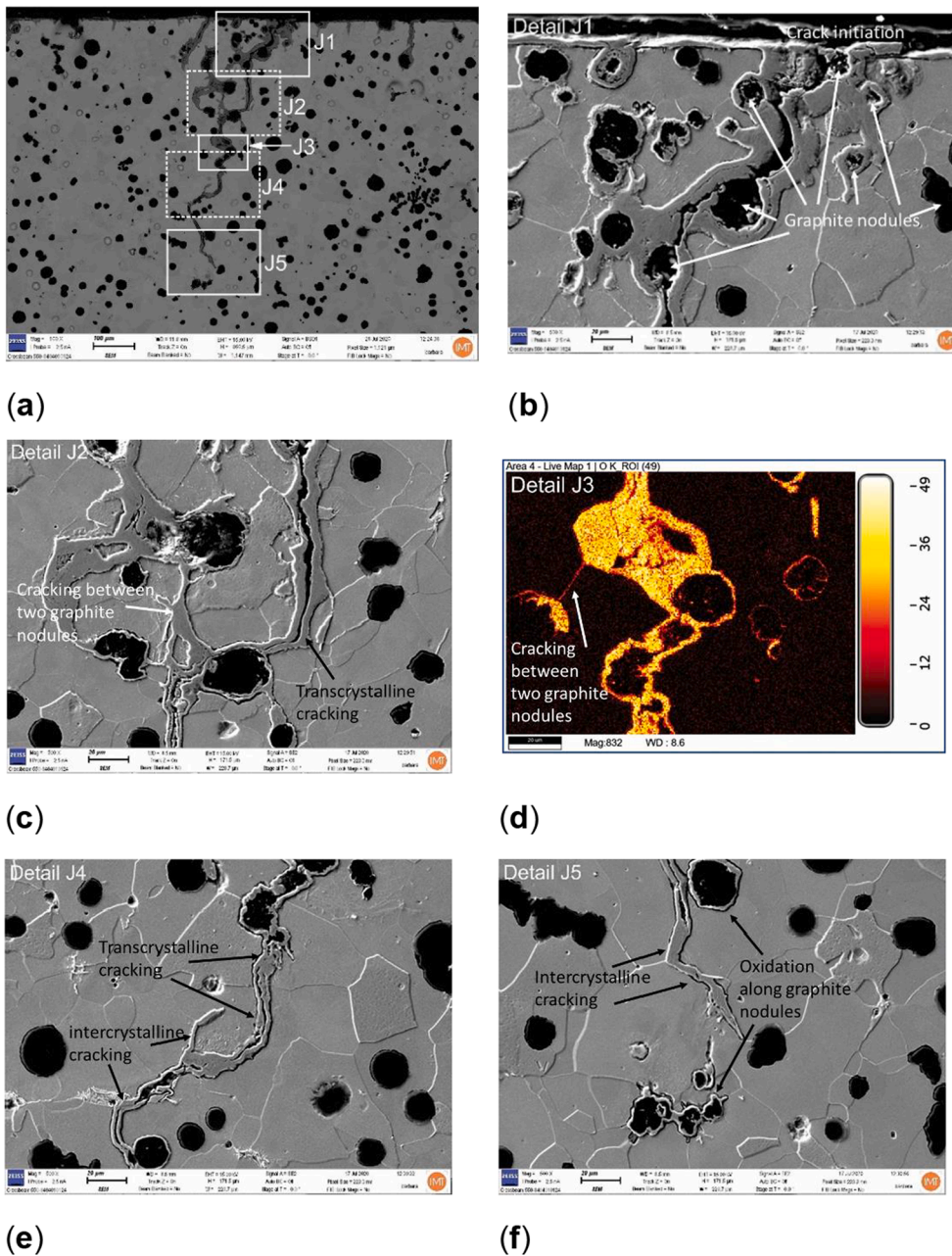


**Fig. 14.** Characteristics at growth of cracks; occurrence of longer crack with denoted spots for **details J1 – J5** (a), **detail J1** for initiation of crack in area of increased graphite density (b), **detail J2** for transcrystalline in grain boundary growth of crack between two graphite nodules (c), **detail J3** mapping of oxygen showing growth of crack from graphite to next graphite with their very low mutual distance (d), **details J4-15** growth of cracks from graphite to another graphite using grain boundary and transcrystalline pathways (e-f), 4000 thermal cycles, all images were made with FEG-SEM ThermoFisher Scientific Quattro S.

thermal fatigue so far.

**3.3.2. Role of pearlite in crack growth**

The role of pearlite in the growth of cracks at elevated temperatures (600 °C) has not been clearly understood. In Fig. 15a, b, several cracks are presented where pearlite is involved in their growth. **Detail K1** in Fig. 15c highlights the area where pearlite is present, and Fig. 15d shows the oxygen mapping for this detail. The spots denoted in Fig. 15c represent areas where pearlite is located, and Fig. 15d displays the initiation of oxidation in these marked pearlite areas, while the vicinity around the pearlite is not subjected to the oxidation process. Oxygen penetration occurs predominantly through grain boundaries, as seen in the oxidized grain boundary in the

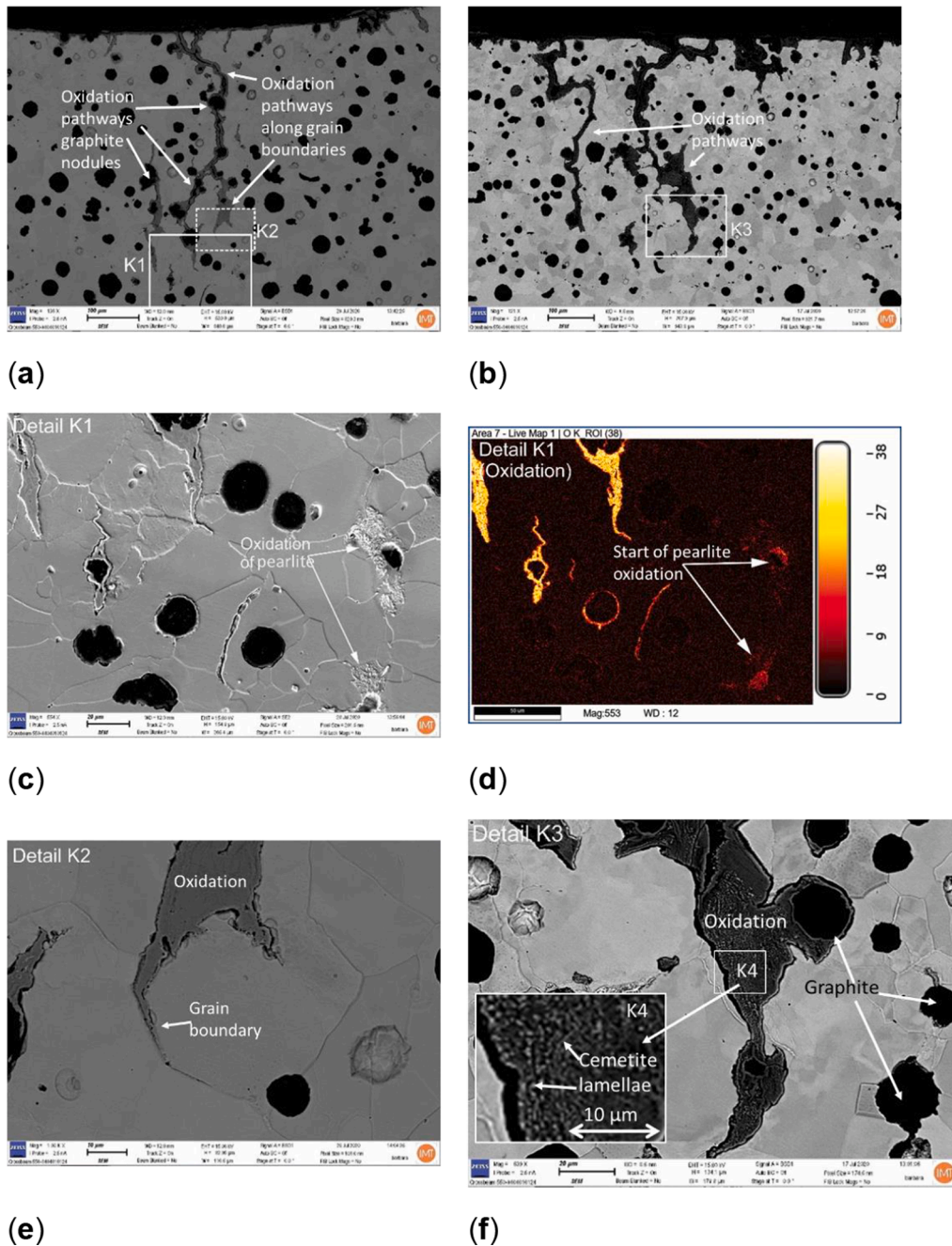


**Fig. 15.** Role of pearlite areas at growth of cracks; growth of cracks including pearlite areas with denoted spots for **details K1 – K4** (a, b and f), **detail K1** showing pearlite areas (c), mapping of oxygen for **detail K1** showing initiation of oxidation of pearlite areas (d), **detail K2** for final stage of oxidation of pearlite area and growth of cracks using grain boundary in transcrystalline pathways (e) and **detail K3** for stage before completely oxidation of pearlite area with visible non-completely oxidized cementite lamellae, with enlarged detail in **K4** (f), all images were made with FIB-SEM Zeiss CrossBeam 550.

vicinity of the pearlite areas in Fig. 15d. The figure also shows the initiation of oxidation around the graphite.

Fig. 15e (detail K2) presents an advanced stage of oxidation in the pearlite areas, while Fig. 15f (detail K3) shows a stage just before complete oxidation of the pearlite area, where the cementite lamellae are not completely oxidized, see detail K4. This is similar to the observations of pearlite in Fig. 8g, h. Furthermore, Fig. 15e shows further growth of cracks, where they propagate through both grain boundary and transcrystalline pathways. The preferential oxidation of pearlite areas compared to the matrix increases the growth of cracks. The preferential oxidation of ferrite in pearlite is obvious, however, this infers that, due to the depletion of carbide forming elements (especially Cr), the eutectoid ferrite lamellas are even more susceptible to oxidation than a fully ferritic matrix.



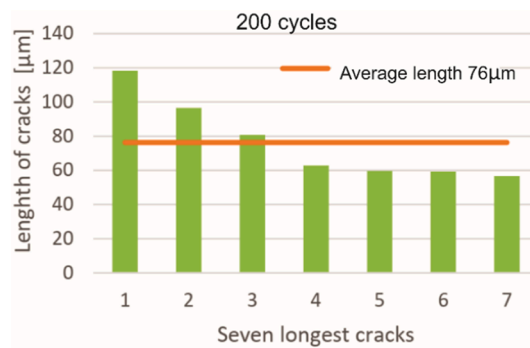


Fig. 17. Lengths of seven longest cracks and average length at 200 cycles.

#### 4. Conclusions

The thermal fatigue tests were conducted on ductile cast iron (DCI) under harsh oxidation conditions. Here are the conclusions that can be derived from the study:

1. Cracking and oxidation of graphite, pearlite islets, grain boundaries and the matrix between graphite nodules are the main degradation mechanisms.
2. Based on their composition, two types of graphite can be distinguished: degenerated (serrated or sharp-edged surfaces, and with ferrite particles in the graphite nodules) and normal (without visible ferrite particles). Degenerated nodules are more susceptible to degradation.
3. Cracks form at locations of stress concentration on graphite surfaces, and a crack network is formed by linking cracks that form on graphite nodules.
4. The degradation mode of graphite depends on their location, and characteristics. Degradation of graphite begins with the oxidation of the graphite-matrix interface, followed by internal oxidation using ferrite particles as pathways.
5. Cracks occur mainly on graphite nodules larger than 15  $\mu\text{m}$  and located at the surface, especially with increased local number density at the cooled surface.
6. Graphite nodules located below the cooled surface experience debonding between the graphite and matrix, which accelerates the growth and oxidation of external cracks, especially when they are closely arranged.
7. Pearlite areas contribute to the degradation of the surface layer and crack growth. Cracking of cementite lamellae in pearlite accelerates their oxidation and increases stresses in the vicinity.
8. Faster crack growth occurs in the case of successively arranged graphite nodules in the radial direction and at shorter distances between the nodules. Cracks can grow by both transcrystalline and intercrystalline pathways.

These conclusions highlight the complex nature of the degradation processes observed in the nodular cast iron during thermal fatigue testing and provide insight into the factors affecting crack growth and oxidation behavior of the material.

#### Funding

The authors would like to thank A. Penko for technical support with thermal fatigue tests. This work was supported by the Slovenian Research Agency (ARRS) under program grants P2-0344 and P2-0268.

#### Declaration of Competing Interest

The authors declare that they have no known competing financial interests or personal relationships that could have appeared to influence the work reported in this paper.

#### Data availability

No data was used for the research described in the article.

#### References

- [1] J.R. Davis (Ed.), *ASM Specialty Handbook—Cast Irons*, ASM International, Metals Park, OH, 1996.
- [2] S. Pan, Y.u. Gang, X. He, S. Li, Y. Zhang, Q. Li, Collective evolution of surface microcrack for compacted graphite iron under thermal fatigue with variable amplitude, *Int. J. Fatigue* 118 (2019) 139–149, <https://doi.org/10.1016/j.ijfatigue.2018.09.005>.
- [3] S.L. Sugwon Kim, A.M.O. Cockcroft, Optimization of the process parameters affecting the microstructures and properties of compacted graphite iron, *J. Alloy. Compd.* 476 (2009) 728–732.

- [4] S. Méndez, M.Á. Arenas, A. Niklas, R. González, A. Conde, J. Sertucha, J.J. de Damborenea, Effect of silicon and graphite degeneration on high-temperature oxidation of ductile cast irons in open air, *Oxid. Met.* 91 (2019) 225–242, <https://doi.org/10.1007/s11085-018-9875-0>.
- [5] C. Ripplinger, M. Gastens, J. Zimmermann, B. Pustal, C. Broeckmann, K.U. Schröder, A. Bührig-Polaczek, Potential of metallurgical gradients in the design of structural components made of nodular cast, *Materials* 14 (2021) 2411, <https://doi.org/10.3390/ma14092411>.
- [6] S. Weitao, W. Bin, L. Xiaoliang, W. Yuqian, Z. Jian, Controlling the tribology performance of gray cast iron by tailoring the microstructure, *Tribol. Int.* (2021), <https://doi.org/10.1016/j.triboint.2021.107343> in print.
- [7] D. Wollmann, G. Pintaude, Tribological performance of high-strength cast iron in lubricated contact containing carbon black, *Wear* 476 (2021), 203743, <https://doi.org/10.1016/j.wear.2021.203743>.
- [8] M.-B. Lin, C.-J. Wang, A.A. Volinsky, High temperature oxidation behavior of flake and spheroidal graphite cast irons, *Oxid. Met.* 76 (2011) 161–168, <https://doi.org/10.1007/s11085-011-9244-8>.
- [9] Y. Liu, Y. Li, J. Xing, S. Wang, B. Zheng, D. Tao, W. Li, Effect of graphite morphology on the tensile strength and thermal conductivity of cast iron, *Mater Charact* 144 (2018) 155–165, <https://doi.org/10.1016/j.matchar.2018.07.001>.
- [10] R. González-Martínez, U. de la Torre, J. Lacaze, J. Sertuch, Effects of high silicon contents on graphite morphology and room temperature mechanical properties of as-cast ferritic ductile cast irons. Part I - Microstructure, *Mater. Sci. Eng. A* 712 (2018) 794–802, <https://doi.org/10.1016/j.msea.2017.11.050>.
- [11] R. González-Martínez, U. de la Torre, A. Ebel, J. Lacaze, J. Sertuch, Effects of high silicon contents on graphite morphology and room temperature mechanical properties of as-cast ferritic ductile cast irons. Part II - Mechanical properties, *Mater. Sci. Eng. A* 712 (2017) 803–811, <https://doi.org/10.1016/j.msea.2017.11.051>.
- [12] L.M. Heine, A. Bezold, C. Broeckmann, Long crack growth and crack closure in high strength nodular cast iron, *Eng. Fract. Mech.* 192 (2018) 24–53, <https://doi.org/10.1016/j.engfracmech.2018.02.003>.
- [13] T. Ikeda, N.A. Noda, Yoshikazu Sano, Conditions for notch strength to be higher than static tensile strength in high-strength ductile cast iron, *Eng. Fract. Mech.* 206 (2019) 75–88, <https://doi.org/10.1016/j.engfracmech.2018.11.034>.
- [14] W. Baer, Chunky graphite in ferritic spheroidal graphite cast iron: formation, prevention, characterization, impact on properties: an overview, *International Journal of Metalcasting* 14 (2020) 454–488, <https://doi.org/10.1007/s40962-019-00363-8>.
- [15] S. Schoenborn, H. Kaufmann, C.M. Sonsino, R. Heim, Variable amplitude fatigue of high-strength cast iron alloys for automotive applications, *Int. J. Fatigue* 91 (2016) 445–458, <https://doi.org/10.1016/j.ijfatigue.2016.01.006>.
- [16] D. Medynski, B.a. Samociuk, A. Janus, J. Chechmanowski, Effect of Cr, Mo and Al on microstructure, abrasive wear and corrosion resistance of Ni-Mn-Cu Cast iron, *Materials* 12 (2019) 3500, <https://doi.org/10.3390/ma12213500>.
- [17] J. Hosdez, N. Limodin, D. Najjar, J.-F. Witz, E. Charkaluk, P. Osmond, A. Forré, F. Szymtka, Fatigue crack growth in compacted and spheroidal graphite cast irons, *Int. J. Fatigue* 131 (2020), 105319, <https://doi.org/10.1016/j.ijfatigue.2019.105319>.
- [18] A. Vaško, Comparison of mechanical and fatigue properties of SiMo- and SiCu types of nodular cast iron, *Mater. Today.. Proc.* 32 (2020) 168–173, <https://doi.org/10.1016/j.matpr.2020.04.184>.
- [19] F. Iacoviello, V. Di Cocco, C. Bellini, Fatigue crack propagation and damaging micromechanisms in Ductile Cast Irons, *Int. J. Fatigue* 124 (2019) 48–54, <https://doi.org/10.1016/j.ijfatigue.2019.02.030>.
- [20] M. Cavallini, O. Di Bartolomeo, F. Iacoviello, Fatigue crack propagation damaging micromechanisms in ductile cast irons, *Eng. Fract. Mech.* 75 (3–4) (2008) 694–704, <https://doi.org/10.1016/j.engfracmech.2007.02.002>.
- [21] V. Di Cocco, F. Iacoviello, Ductile cast irons: Microstructure influence on the damaging micromechanisms in overloaded fatigue cracks, *Eng. Fail. Anal.* 82 (2017) 340–349, <https://doi.org/10.1016/j.engfailanal.2017.06.039>.
- [22] F. Iacoviello, V. Di Cocco, C. Bellini, Overload effects on fatigue cracks in a ferritized ductile cast iron, *Int. J. Fatigue* 127 (2019) 376–381, <https://doi.org/10.1016/j.ijfatigue.2019.06.028>.
- [23] R. Konečná, G. Nicoletto, L. Bubenko, S. Fintová, A comparative study of the fatigue behavior of two heat-treated nodular cast irons, *Eng. Fract. Mech.* 108 (2013) 251–262, <https://doi.org/10.1016/j.engfracmech.2013.04.017>.
- [24] S. Vantadori, C. Ronchei, D. Scorza, A. Zanichelli, A. Carpinteri, Fatigue behaviour assessment of ductile cast iron smooth specimens, *Int. J. Fatigue* 152 (2021), 106459, <https://doi.org/10.1016/j.ijfatigue.2021.106459>.
- [25] C.L. Zou, J.C. Pang, M.X. Zhang, et al., The high cycle fatigue, deformation and fracture of compacted graphite iron: influence of temperature, *Mater. Sci. Eng. A* 724 (2018) 606–615, <https://doi.org/10.1016/j.msea.2018.01.025>.
- [26] X.J. Wu, G. Quan, R. MacNeil, et al., Failure mechanisms and damage model of ductile cast iron Under low-cycle fatigue conditions, *Metall. Mater. Trans. A* 45 (11) (2014) 5085–5097, <https://doi.org/10.1007/s11661-014-2468-x>.
- [27] P. Canžar, Z. Tonković, J. Kodvanj, Microstructure influence on fatigue behaviour of nodular cast iron, *Mater. Sci. Eng. A* 556 (2012) 88–99, <https://doi.org/10.1016/j.msea.2012.06.062>.
- [28] V. Norman, P. Skoglund, D. Leidermark, J. Moverare, Damage mechanisms in silicon-molybdenum cast irons subjected to thermo-mechanical fatigue, *Int. J. Fatigue* 99 (2017) 258–265, <https://doi.org/10.1016/j.ijfatigue.2017.01.014>.
- [29] C.L. Zou, L.J. Chen, J.C. Pang, M. Wang, Y. Qiu, S.X. Li, Z.F. Zhang, The low-cycle fatigue, fracture and life prediction of compacted graphite iron: Influence of temperature, *Mater. Sci. Eng. A* 724 (2018) 606–615, <https://doi.org/10.1016/j.msea.2019.138101>.
- [30] Y.-J. Kim, H.o. Jang, O.h. Yong-Jjun, High-temperature low-cycle fatigue property of heat-resistant ductile-cast irons, *Metal. Mater. Transact.* 40a/9 (2009) 2087, <https://doi.org/10.1007/s11661-009-9911-4>.
- [31] M.X. Zhang, J.C. Pang, Y. Qiu, S.X. Li, M. Wang, Z.F. Zhang, Thermo-mechanical fatigue property and life prediction of vermicular graphite iron, *Mater. Sci. Eng. A* 698 (2017) 63–72, <https://doi.org/10.1016/j.msea.2017.05.035>.
- [32] M.X. Zhang, J.C. Pang, Y. Qiu, S.X. Li, M. Wang, Z.F. Zhang, Influence of microstructure on the thermo-mechanical fatigue behavior and life of vermicular graphite cast irons, *Mater. Sci. Eng. A* 771 (2020) 138617, <https://doi.org/10.1016/j.msea.2019.138617>.
- [33] E. Kihlberg, V. Norman, P. Skoglund, P. Schmidt, J. Moverare, On the correlation between microstructural parameters and the thermo-mechanical fatigue performance of cast iron, *Int. J. Fatigue* 145 (2021), 106112, <https://doi.org/10.1016/j.ijfatigue.2020.106112>.
- [34] X.J. Wu, G. Quan, R. MacNeil, et al., Thermomechanical fatigue of ductile cast iron and its life prediction, *Metall. Mater. Trans. A* 46 (2015) 2530–2543.
- [35] E. Hosseini, S.R. Holdsworth, Cracking due to combined TMF and HCF loading in cast iron, *Int. J. Fatigue* 99 (2017) 279–285, <https://doi.org/10.1016/j.ijfatigue.2016.10.014>.
- [36] V. Norman, P. Skoglund, D. Leidermark, J. Moverare, The effect of superimposed high-cycle fatigue on thermo-mechanical fatigue in cast iron, *Int. J. Fatigue* 88 (2016) 121–131, <https://doi.org/10.1016/j.ijfatigue.2016.03.020>.
- [37] V.L. Diaconu, T. Sjogren, P. Skoglund, et al., Influence of molybdenum alloying on thermomechanical fatigue life of compacted graphite irons, *Int. J. Cast Metals Res.* 25 (2012) 277–286.
- [38] Y. Qiu, J.C. Pang, S.X. Li, M.X. Zhang, Z.F. Zhang, Influence of temperature on the low-cycle fatigue properties of compacted graphite iron, *Int. J. Fatigue* 117 (2018) 450–460, <https://doi.org/10.1016/j.ijfatigue.2018.08.031>.
- [39] S. Xiang, P. Hedström, B. Zhub, J. Linder, J. Odqvist, Influence of graphite morphology on the corrosion-fatigue properties of the ferritic Si-Mo-Al cast iron SiMo1000, *Int. J. Fatigue* 140 (2020), 105781, <https://doi.org/10.1016/j.ijfatigue.2020.105781>.
- [40] S.N. Lekakh, M. Buchely, R. O'Malley, L. Godlewski, Mei Li, Thermo-cycling fatigue of SiMo ductile iron using a modified thermo-mechanical test, *Int. J. Fatigue* 148 (2021), 106218, <https://doi.org/10.1016/j.ijfatigue.2021.106218>.
- [41] Y. Yun-long, C. Zhan-yi, L. Zhen-song, Y. Hai-Xia, Thermal fatigue behavior and cracking characteristics of high Si-Mo nodular cast iron for exhaust manifolds, *J. Iron Steel Res. Int.* 20 (6) (2013) 52–57, [https://doi.org/10.1016/S1006-706X\(13\)60111-9](https://doi.org/10.1016/S1006-706X(13)60111-9).
- [42] X. Tong, H. Zhou, L.-Q. Ren, Z.-H. Zhang, W. Zhang, R.-D. Cui, Effects of graphite shape on thermal fatigue resistance of cast iron with biomimetic non-smooth surface, *Int. J. Fatigue* 31 (2009) 668–677, <https://doi.org/10.1016/j.ijfatigue.2008.03.023>.

- [43] X. Tong, H. Zhou, L.-Q. Ren, Z.-H. Zhang, R.-D. Cui, W. Zhang, Thermal fatigue characteristics of gray cast iron with non-smooth surface treated by laser alloying of Cr powder, *Surf. Coat. Technol.* 202 (2008) 2527–2534, <https://doi.org/10.1016/j.surfcoat.2007.09.014>.
- [44] X.S. Wang, W.Z. Zhang, B. Guo, Investigation on the thermal crack evolution and oxidation effect of compacted graphite iron under thermal shock, *J. Mater. Eng. Perform.* 24 (9) (2015) 3419, <https://doi.org/10.1007/s11665-015-1641-8>.
- [45] X.S. Wang, W.Z. Zhang, Oxidation and thermal cracking behavior of compacted graphite iron under high temperature and thermal shock, *Oxid. Met.* 87 (2017) 179–188, <https://doi.org/10.1007/s11085-016-9664-6>.
- [46] X. Wang, Weizheng Zhang, Bingbin Guo, Weimao Zhao, The characteristics of microcrack initiation process in cast iron materials under thermal shock test, *Mater. Sci. Eng. A* 609 (2014) 310–317, <https://doi.org/10.1016/j.msea.2014.05.012>.
- [47] M.X. Zhang, J.C. Pang, L.J. Meng, S.X. Li, Q.Y. Liu, A.L. Jiang, Z.F. Zhang, Study on thermal fatigue behaviors of two kinds of vermicular graphite cast irons, *Mater. Sci. Eng. A* 814 (2021), 141212, <https://doi.org/10.1016/j.msea.2021.141212>.
- [48] D. Bombač, G. Kugler, B. Markoli, M. Terčelj, Hot work roller surface layer degradation progress during thermal fatigue in the temperature range 500–700 °C, *Int. J. Fatigue* 104 (2017) 355–365, <https://doi.org/10.1016/j.ijfatigue.2017.08.008>.
- [49] D. Bombač, G. Kugler, Jaka Burja, Milan Terčelj, Early spalling analysis of large particles in high-Cr steel during thermal fatigue: relevant mechanisms, *Materials* 15 (2022) 6705, <https://doi.org/10.3390/ma15196705>.
- [50] D. Bombač, M.G.G. Kugler, M. Terčelj, Mechanisms of oxidation degradation of Cr12 roller steel during thermal fatigue tests, *Metals* 10 (4) (2020) 450–468, <https://www.mdpi.com/2075-4701/10/4/450>.
- [51] P. Chen, Z. Liu, R. Li, X. Li, The effect of manganese additions on the high temperature oxidation behaviour of the high-vanadium cast iron, *J. Alloys Compounds* 767 (2018) 181–187, <https://doi.org/10.1016/j.jallcom.2018.07.113>.
- [52] Z. Zhu, H. Xu, D. Jiang, X. Mao, N. Zhang, Influence of temperature on the oxidation behaviour of a ferritic-martensitic cast iron in supercritical water, *Corros. Sci.* 113 (2016) 172–179, <https://doi.org/10.1016/j.corsci.2016.10.020>.
- [53] F. Abe, H. Kutsumi, H. Haruyama, H. Okubo, Improvement of oxidation resistance of 9 mass% chromium cast iron for advanced-ultra supercritical power plant boilers by pre-oxidation treatment, *Corros. Sci.* 114 (2017) 1–9, <https://doi.org/10.1016/j.corsci.2016.10.008>.
- [54] X. Zhang, Z. Wang, J. Lin, Z. Zhou, A study on high temperature oxidation behavior of high-velocity arc sprayed Fe-based coatings, *Surf. Coat. Technol.* 283 (2015) 255–261, <https://doi.org/10.1016/j.surfcoat.2015.10.067>.
- [55] P.H. Gao, S.T. Cao, J.P. Li, Z. Yang, Y.C. Guo, Y.R. Wang, High temperature oxidation resistance of M42C stainless cast iron coatings deposited on the surface of cast iron through atmospheric plasma spraying, *J. Alloy. Compd.* 684 (2016) 188–194, <https://doi.org/10.1016/j.jallcom.2016.05.181>.
- [56] M.A.E. Jepson, R.L. Higginson, The influence of microstructure on the oxidation of duplex stainless cast iron in simulated propane combustion products at 1000 °C, *Corros. Sci.* 51 (2009) 588–594, <https://doi.org/10.1016/j.corsci.2008.11.023>.
- [57] Q. Guo, Z. Yang, D. Guo, D. Tao, Y. Guo, J. Li, Y. Bai, Research on the oxidation mechanism of vermicular graphite cast iron, *Materials* 12 (2019) 3130, <https://doi.org/10.3390/ma12193130>.
- [58] W.u. Yue, J. Li, Z. Yang, Y. Guo, Z. Ma, M. Liang, T. Yang, D. Tao, Creep behavior accompanying oxidation of compacted graphite cast iron, *Mater. Sci. Eng. A* 723 (2018) 174–181, <https://doi.org/10.1016/j.msea.2018.03.039>.
- [59] B. Panicaud, J.L. Grosseau-Poussard, J.F. Dinhut, On the growth strain origin and stress evolution prediction during oxidation of metals, *Appl. Surf. Sci.* 252 (16) (2006) 5700–5713.
- [60] F. Yang, B. Liu, D.N. Fang, Analysis on high-temperature oxidation and growth stress of iron-based alloy using phase field method, *Appl. Math. Mech. (eng.ed.)* 32 (6) (2011) 757–764.
- [61] J.W. Chen, Z. Jiang, H. Mu, Q. Wan, L. Hu, B. Yang, Simulation on the thermal stress of super 304H oxidation scale at 600°C, *Adv. Mater. Res.* 1065–1069 (2014) 1934–1938.
- [62] M. Stawarz and P. M. Nuckowski, Corrosion Behavior of SiMo Cast Iron under Controlled Conditions, doi: 10.3390/ma15093225.
- [63] Q. Shi, J. Liu, W. Wang, W. Yan, Y. Shan, K. Yang, High temperature oxidation behavior of SIMP cast iron, *Oxid. Metals* 83 (2015) 521–532, <https://doi.org/10.1007/s11085-015-9532-9>.
- [64] D.S. Li, D. Li, H. Dou, P. Gao, Y. Liu, X.J. Chen, et al., High-temperature oxidation resistance of austenitic stainless cast iron, *Key Eng. Mater.* 575–576 (2013) 414–417.
- [65] K. Kusumoto, X. Shimizu, H. Yaer, K. Hara, H. Tamura, Kawai, High erosionoxidation performance of Fe-based Nb or V containing multi-component alloys with Co addition at 1173K, *Mater. Des.* 88 (2015) 366–374, <https://doi.org/10.1016/j.matdes.2015.08.161>.
- [66] S. Ghodrati, M. Janssen, L.A.I. Kestens, J. Sietsma, Volume expansion of compacted graphite iron induced by pearlite decomposition and the effect of oxidation at elevated temperature, *Oxid. Met.* 80 (2013) 161–176, <https://doi.org/10.1007/s11085-013-9406-y>.
- [67] A. Ebel, O. Marsan, J. Lacaze, B. Malard, Cyclic oxidation of high-silicon spheroidal graphite iron, *Corros. Sci.* 192 (2021), 109854, <https://doi.org/10.1016/j.corsci.2021.109854>.
- [68] A. Ebel, S.Y. Brou, B. Malard, J. Lacaze, D. Monceau, L. Vaissière, High-temperature oxidation of a high silicon SiMo spheroidal cast iron in air with in situ change in H<sub>2</sub>O content, *Mater. Sci. Forum* 925 (2018) 353–360, <https://doi.org/10.4028/www.scientific.net/MSF.925.353>.
- [69] S.N. Lekakh, C. Johnson, A. Bofah, L. Godlewski, M. Li, Improving high-temperature performance of high Si-alloyed ductile iron by altering additions, *Int. J. Metalcasting* 15 (3) (2021) 874–888, <https://doi.org/10.1007/s40962-020-00524-0>.
- [70] S.N. Lekakh, W. Tucker, A. Bofah, T. Selly, T. Godlewski, M. Li, Quantitative  $\mu$ -CT analysis of scale topology formed during oxidation of high SiMo cast iron, *Oxid. Met.* 94 (2020) 251–264, <https://doi.org/10.1007/s11085-020-09989-0>.
- [71] M.P. Brady, G. Muralidharan, D.N. Leonard, J.A. Haynes, R.G. Weldon, R.D. England, Long-term oxidation of candidate cast iron and stainless steel exhaust system alloys from 650 to 800 °C in air with water vapor, *Oxid. Met.* 82 (2014) 359–381, <https://doi.org/10.1007/s11085-014-9496-1>.
- [72] S.N. Lekakh, A. Bofah, W.T. Chen, L. Godlewski, M. Li, Prevention of high-temperature surface degradation in SiMo cast irons by Cr and Al alloying, *Metall. Mater. Trans. B* 51B (2020) 2542–2554, <https://doi.org/10.1007/s11663-020-01975-w>.
- [73] M. Ekström, P. Szakalos, Jonsson, Influence of Cr and Ni on high-temperature corrosion behavior of ferritic ductile cast iron in air and exhaust gases, *Oxid. Met.* 80 (2013) 455–466, <https://doi.org/10.1007/s11085-013-9389-8>.
- [74] S. Pan, F. Zeng, S.u. Nanguang, Z. Xian, The effect of niobium addition on the microstructure and properties of cast iron used in cylinder head, *J. Mater. Res. Technol.* 9 (2) (2020) 1509–1518, <https://doi.org/10.1016/j.jmrt.2019.11.076>.
- [75] A. Ebel, M. Alves Pegoraro, B. Malard, C. Tenaillon, J. Lacaze, Coarsening and dendritic instability of spheroidal graphite in high silicon cast iron under thermal cycling in the ferritic domain, *Scripta Comput. Sci. Appl. Math. Materialia* 178 (2020) 86–89, <https://doi.org/10.1016/j.scriptamat.2019.11.001>.
- [76] M. Alves Pegoraro, C. Tenaillon, A. Ebel, B. Malard, J. Lacaze, Spheroidal graphite coalescence during thermal cycling in the ferritic domain of a high-silicon cast iron studied by optical microscopy and X-ray computed tomography, *Mater. Today Commun.* 25 (2020), <https://doi.org/10.1016/j.mtcomm.2020.101422>.
- [77] G. Hütter, L. Zybelle, M. Kuna, Micromechanisms of fracture in nodular cast iron: From experimental findings towards modeling strategies – A review, *Eng. Fract. Mech.* 144 (2015) 118–141, <https://doi.org/10.1016/j.engfractmech.2015.06.042>.
- [78] C. Gebhardt, J. Zhang, A. Bezold, C. Broeckmann, Microscale fatigue mechanisms in high silicon alloyed nodular cast iron, *IJ Fatigue* 168 (2023), 107402, <https://doi.org/10.1016/j.ijfatigue.2022.107402>.
- [79] S. Xiang, P. Hedström, B. Zhu, J. Linder, J. Odqvist, Influence of graphite morphology on the corrosion-fatigue properties of the ferritic Si-Mo-Al cast iron SiMo1000, *IJ Fatigue* 140 (2020), 105781, <https://doi.org/10.1016/j.ijfatigue.2020.105781>.
- [80] C.L. Zou, J.C. Pang, M.X. Zhang, Y. Qiu, S.X. Li, L.J. Chen, J.P. Li, Z. Yang, Z.F. Zhang, The high cycle fatigue, deformation and fracture of compacted graphite iron influenced by temperature, *Mater. Sci. Eng. A* 724 (2018) 606–615, <https://doi.org/10.1016/j.msea.2018.01.025>.
- [81] W.u. Yue, J. Li, H.a. Chen, Z. Yang, Y. Guo, M. Liang, Study on the impact wear mechanism and damage modes of compacted graphite cast iron, *J. Mater. Res. Technol.* 21 (11–12) (2022) 4002–4011, <https://doi.org/10.1016/j.jmrt.2022.10.102>.
- [82] W. Skudlarek, M.N. Krmasha, K.S. Al-Rubaie, O. Preti, J.C.G. Milan, C.E. da Costa, Effect of austempering temperature on microstructure and mechanical properties of ductile cast iron modified by niobium, *J. Mater. Res. Technol.* 12 (2021) 2414–2425, <https://doi.org/10.1016/j.jmrt.2021.04.041>.

- [83] L. Gong, F.u. Hanguang, P. Yang, X. Ji, W. Yin, J. Lin, Refinement of primary carbides and improvement of wear resistance of hypereutectic high chromium cast iron after modification, *J. Mater. Res. Technol.* 24 (2023) 5724–5742, <https://doi.org/10.1016/j.jmrt.2023.04.176>.
- [84] B.-H. Zhang, H.-N. Li, N.-B. Yuan, G.-Y. Qiao, Fu-ren Xiao, Influence of adding Nb on oxidation resistance of hypoeutectic high-chromium cast iron, *J. Mater. Res. Technol.* (2023), <https://doi.org/10.1016/j.jmrt.2023.08.295>.
- [85] Geraldo Lúcio de Faria, Paulo Sérgio Moreira, Rodrigo Rangel Porcaro, Ana Paula Moreira Barboza, Tamires Cristiane Valadares Silva, Development of an oxidation contrast method for pearlite colony revelation in eutectoid steels, metallography, microstructure, and analysis, *ChemistrySelect* 10 (2021) 589–600, <https://doi.org/10.1007/s13632-021-00780-4>.
- [86] H.K. Mehtani, M.I. Khan, A. Durgaprasada, S.K. Debb, S. Parida, M.J.N.V. Prasad, I. Samajdar, Oxidation kinetics in pearlite: The defining role of interface crystallography, *Scripta Comput. Sci. Appl. Math. Mater.* 152 (2018) 44–48, <https://doi.org/10.1016/j.scriptamat.2018.04.011>.